Available online at www.sciencedirect.com
ScienceDirect
International Journal of Solids and Structures 45 (2008) 4068–4097
INTERNATIONAL JOURNAL OF SOLIDS AND STRUCTURES
www.elsevier.com/locate/ijsolstr

Refinements of damage detection methods based on wavelet analysis of dynamical shapes

Arcangelo Messina *

Dipartimento di Ingegneria dell'Innovazione, Università del Salento, Via per Monteroni, 73100 Lecce, Italy

Received 7 September 2007; received in revised form 12 January 2008
Available online 29 February 2008

Abstract

This manuscript aims at illustrating significant refinements concerning the use of wavelets, when these latter are used in the guise of continuous wavelet transforms (CWT) for identifying damage on transversally vibrating structural components (e.g. beams, plates and shells). The refinements regard the presentation of wavelet-algorithms which are aimed at significantly reducing those border distortions normally arising during a wavelet-damage detection procedure. The main advantage of the algorithms is that they are self-contained, namely: (i) the wavelet transforms do not undergo any own variation and their application follows the convolution laws established in the past; (ii) it is not necessary to design a specific boundary wavelet; (iii) no significant analytical treatment neither of the wavelets nor of the signal is required and, finally, (iv) the algorithms can be adapted to different boundary conditions and different physical situations. Besides all the specified advantages, the wavelet-damage detection procedure is still carried out by excluding historical data. The effectiveness of the algorithms is shown through numerical and experimental examples. These latter are illustrated along with reduced outliers of experimental estimation through a related consistent statistical procedure.

Keywords: Open cracks; Vibrating beams and plates; Wavelets; Damage detection; Laser measurements

1. Introduction

Damage detection based on changes of modal data or, more in general, vibration-based data, has become one of the most attractive research topics in recent years (Dimarogonas, 1996; Salawu, 1997; Doebling et al., 1998; Kim and Melhem, 2004). The attraction is mainly due to the possibility of identifying damaged locations by putting aside the knowledge a-priori of the damaged zone. Although such a principle could also be extended to existing NDTs (e.g. Ultrasonic, X-ray, etc. (Reese and Kawahara, 1993; Staszewski et al., 2004)), such an extension is not straightforward for a number of technical and practical reasons. In particular, the mentioned existing ND evaluating techniques should interest point-by-point the whole structure by consuming times and sometimes using costly devices. Staszewski et al. (2004) illustrate an interesting brief summary of these existing ND techniques.

* Tel.: +39 0832 297 801; fax: +39 0832 297 802.
E-mail address: arcangelo.messina@unile.it

0020-7683/$ - see front matter © 2008 Elsevier Ltd. All rights reserved.
doi:10.1016/j.ijsolstr.2008.02.015

The investigation, or the so called damage monitoring and inspection, could, therefore, be based on modal and related vibrational data but, in that case, the global nature of these techniques should be taken into account. Indeed, modal data depend on the physical parameters of the structures under test but such dependency could be considered in nature as *macro* rather than *micro* and, therefore, the related sensitivity would be *macro* too. Such an apparent limitation must be sought within the frequency range where the modal data are usually measured (low frequency: a few kHz); in such circumstances the boundary within which the modal data begin to provide interesting sensitivities depends on several factors: the system under test, the measuring devices and the amount of damage which deserves to be taken into account. Apart from these possible limitations, which could be tackled and to a certain extent overcome when used in junction with the most modern technology, the attractions offered by the techniques based on modal data deserve to be appropriately investigated.

This work deals with the methods that try to detect the existence and location of damage through the processing of dynamical shapes strictly related to the system under test (SUT). Therefore, the monitoring technique herein dealt with does not need a mathematical model of the system but it only needs measured inherent data (i.e. dynamical shape). In this regard, several researchers have recently followed this approach by using several approaches (e.g. Yuen, 1985; Pandey et al., 1991; Ratcliffe, 1997; Ratcliffe and Bagaria, 1998; Wang and Deng, 1999; Hong et al., 2002; Gentile and Messina, 2002, 2003; Loutridis et al., 2004; Messina, 2004; Han et al., 2005; Yoon et al., 2005; Rucka and Wilde, 2006a,b; Trentadue et al., 2007) and among them the application of wavelet analysis is one of the most investigated subjects. The present context regards the wavelet analysis applied in the guise of CWT as established in Gentile and Messina (2003) and Messina (2004).

Certain *dynamical shapes* associated to a damaged transversally vibrating structural element (here a beam as a non limiting simplicity) constitute the only information available to the analyst in order to carry out the related inspection on the state of health of the system. In this respect, the analyst, once having carried out the CWT of the measured dynamical shape through an appropriate numerical method, needs to look for local abnormalities along the same transform in order to detect the damaged location. This approach is made attractive by the availability of recent laser-technologies joined to accurate and fast scanning devices which allow to measure point-by-point the dynamic shape of large areas (plates and shells) or lengths (beams).

Within the frame of the mentioned damage detecting approach, the motivation of the present work regards a known phenomenon which can be termed as *border distortion*; this phenomenon consists of abnormal rises of the continuous wavelet transforms occurring at the ends of certain transformed digital dynamical shapes. This phenomenon, as discussed in Gentile and Messina (2003), depends on the boundary conditions and can also be spread on the internal points of the monitored dynamic shape depending on the extent of the analyzing wavelet (the different extent is an essential feature used to minimize the noise (Messina, 2004)); in Gentile and Messina (2003) the phenomenon was also empirically discussed along with certain equivalences between continuous wavelet transforms (CWTs) and classical derivatives, whilst, Messina (2004) also investigated the correlation between continuous wavelet transforms and digital differentiator filters along with the convolution operation of FIR filters.

Because the identification of a damaged location depends on the abnormalities, anything causing abnormalities, but extraneous to the damage, is a potential source for a false indication. Moreover, the importance of reducing the border distortion phenomenon is also due to the fact that the investigated area of the structural element is effectively reduced by the presence of this phenomenon along with the extent of the analyzing wavelet. In such a perspective the so called *border distortion* phenomenon must be reduced in some way.

The *border distortion* phenomenon is also mentioned in Rucka and Wilde (2006a,b) and there also exist works which deal with border effect within the frame of regression analysis (e.g. Oh et al., 2001; Lee and Oh, 2004; Oh and Lee, 2005) and classical works dealing with this specific subject (Strang and Nguyen, 1996; Misiti et al., 2006b). As far as the objectives of the present work are concerned, Rucka and Wilde (2006a,b), Strang and Nguyen (1996) and Misiti et al. (2006b) are particularly relevant; in particular, Rucka and Wilde (2006a,b) suggested an interesting and simple boundary treatment for overcoming the problem: extrapolating cubic spline, based on three (Rucka and Wilde, 2006b) or four (Rucka and Wilde, 2006a) neighbouring points, were essentially considered as the resolution key of the problem.

This work introduces two different methods aimed at reducing the so called *border distortion* phenomenon which can be easily and immediately applied to real data; the methods are characterised by different levels of

complexity and their successful behaviour can be interpreted in the light of the equivalencies between CWT and differentiator FIR filters Messina (2004); all the analytical and experimental tests are based on a highly redundant number of points (a few hundreds) in order to stay in line with the past investigations (Gentile and Messina, 2003; Messina, 2004; Trentadue et al., 2007). The methods presented in this work are discussed in comparison with those already proposed in the open literature whenever existing and, finally, it is believed that all findings herein illustrated are applicable in all structures which allow a multi-grid measurability of dynamical shapes.

2. The system under test and the border distortion

The system taken into account in the present work along with its nomenclature is schematically shown in Fig. 1, where, the system under test (SUT) consists of a beam having clamped-free (CF) boundary conditions. The boundary conditions, the material and further details will be specified when necessary. The analytical–numerical model simulating the damage in a cracked beam is developed in Gentile and Messina (2002) (i.e. open symmetrical crack, without considering the effect of rotatory inertia). As far as experimental dynamical shapes are concerned, the measurements obtained as illustrated in Trentadue et al. (2007) are taken into account. In particular, as far as these latter data are concerned, it is stressed here that a slightly improved method (Messina and Albanese, 2008) has been applied in order to extract dynamical shapes without outliers.

2.1. Border distortion in CWTs

Based on the previous sections and on past studies (Messina, 2004) the CWT and its relevant filtered derivative are estimated through the following numerical convolution law:

$$D_o(w(n);a) = h_o(n,a) * w(n) \tag{1}$$

where D_o is the filtered numerical derivative, being "o" the order of differentiation and $w(n)$ the dynamical shape containing damage information in the samples domain ($n = 0,\ldots,N-1$). In particular, D_o should be intended as a low-passed oth derivative ($d^o w/\mathrm{d}n^o$). The term "a" is the dilation parameter which, once settled to an established natural number, designs the capability of $h_o(n)$ (the convolving filter) to deal with the noise contained within $w(n)$. The dilation will stretch (higher a values) or compress (lower a values) $h_o(n)$ in order to reduce or amplify the noise, respectively; this behavior can also be seen in the Fourier transformed domain (Messina, 2004). The number of taps of the filter $h_o(n)$ corresponds to $N_f = 10a + 1$. Finally, the convolving numerical filters $h_o(n)$ depends on the vanishing moments of the chosen Gaussian wavelets (Mallat, 2001; Gentile and Messina, 2003; Messina, 2004) with the related differentiation which is presented within its physical domain ($x \in [0, L]$ of Fig. 1 in the present context) once D_o (Eq. (1)) has been normalized by $(N/L)^o$.

As far as the border distortion phenomenon is concerned, such a phenomenon arises from the application of Eq. (1). In particular, if the dynamical shape $w(n)$ is sufficiently smooth at the ends the border distortion can also be absent or minimum. Conversely, if the dynamical shape contains non-smooth ends, Eq. (1) causes the presence of abnormal rises in $D_o(w(n); a)$. Such abnormalities can also be extended to the internal points of the beam thus causing false indication in damage identification or shading real damage condition close to borders.

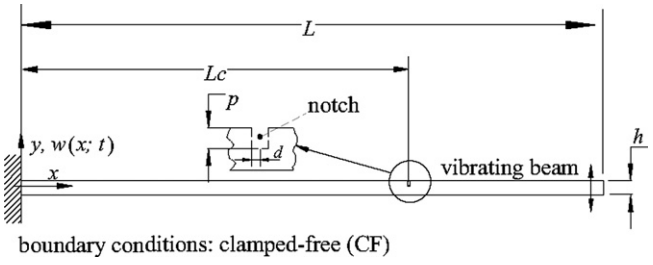

Fig. 1. Nomenclature and geometry of the system under test.

In this work, two methods significantly reducing such a phenomenon, further than aimed at eventually reducing the number of partitions which inefficiently sometimes are requested to investigate a whole system, are presented.

Based on Fig. 1, the border distortion will be analyzed firstly by taking into account mode shapes of an undamaged beam subjected to CC, SS and FF boundary conditions. The data, unless otherwise specified, regard beams having Young's module $E = 6.9$ GPa, density $\rho = 1360$ kg/m^3, thickness $h = 16$ mm, length $L = 570$ mm, damage $p=h/2$; $d = 1$ mm and, finally, a number of measuring points $N = 500$ over mode shapes normalized by assuming unitary the absolute maximum value. Finally, when an analytical mode shape is corrupted by noise this latter is simulated through a Gaussian model having null mean and standard deviation σ through a specified signal to noise ratio $SN_{[dB]} = 20 \log_{10}(|w|_{max}/\sigma)$.

3. Border distortion in CWTs: reduction methods

Figs. 2–4 are able to clearly illustrate and, therefore, quantitatively recall the above mentioned phenomenon of border distortion.

The reason why all Figs. 2–4 take into account 2nd, 3rd and 4th derivatives can be found in literature (Gentile and Messina, 2002; Rucka and Wilde, 2006a,b). Different investigations have pointed out the importance of

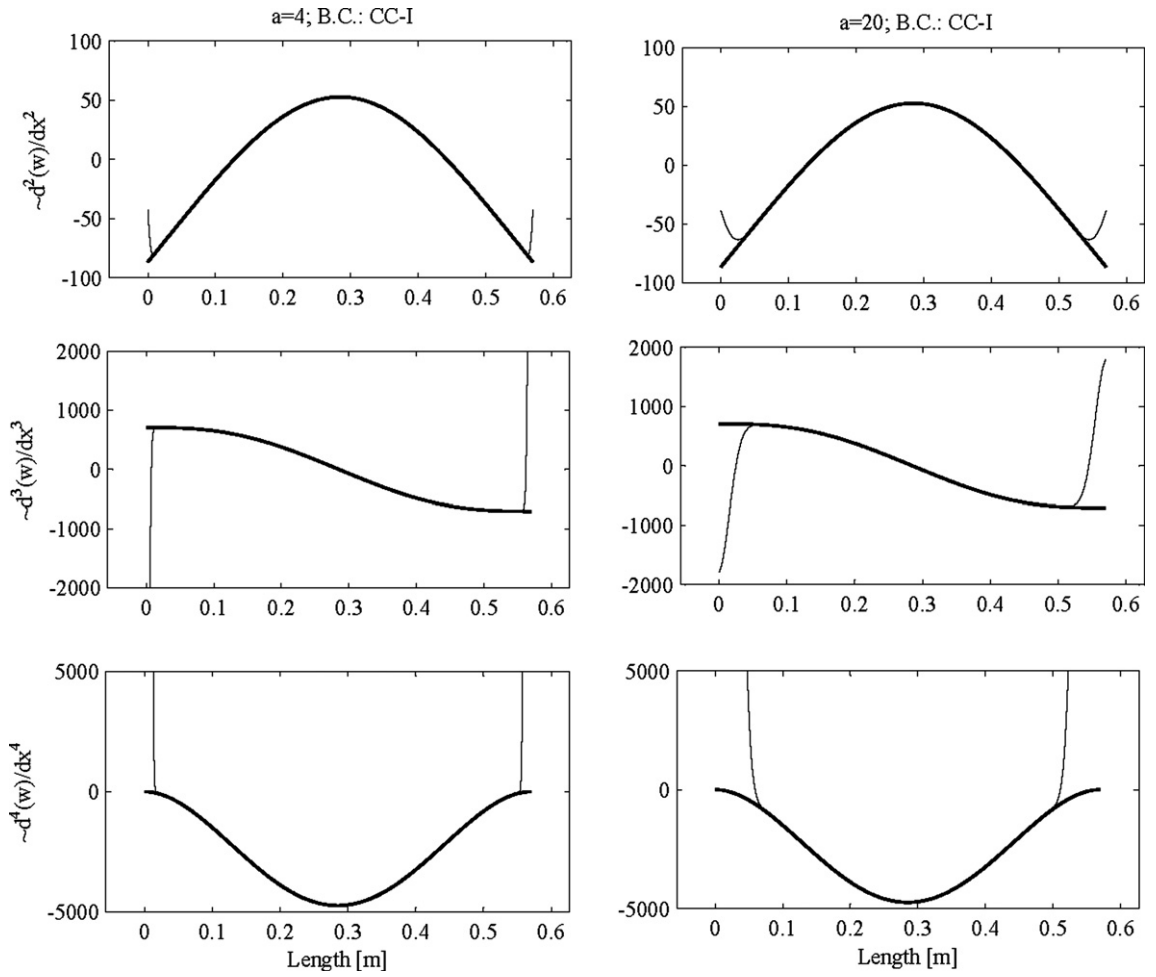

Fig. 2. Border distortion for the first mode shape of an undamaged CC beam (114.02 Hz; based on classical Euler–Bernoulli beam model); influence of different dilation parameters from the second up to the fourth derivative on mode shapes free of noise (bold line: exact derivative).

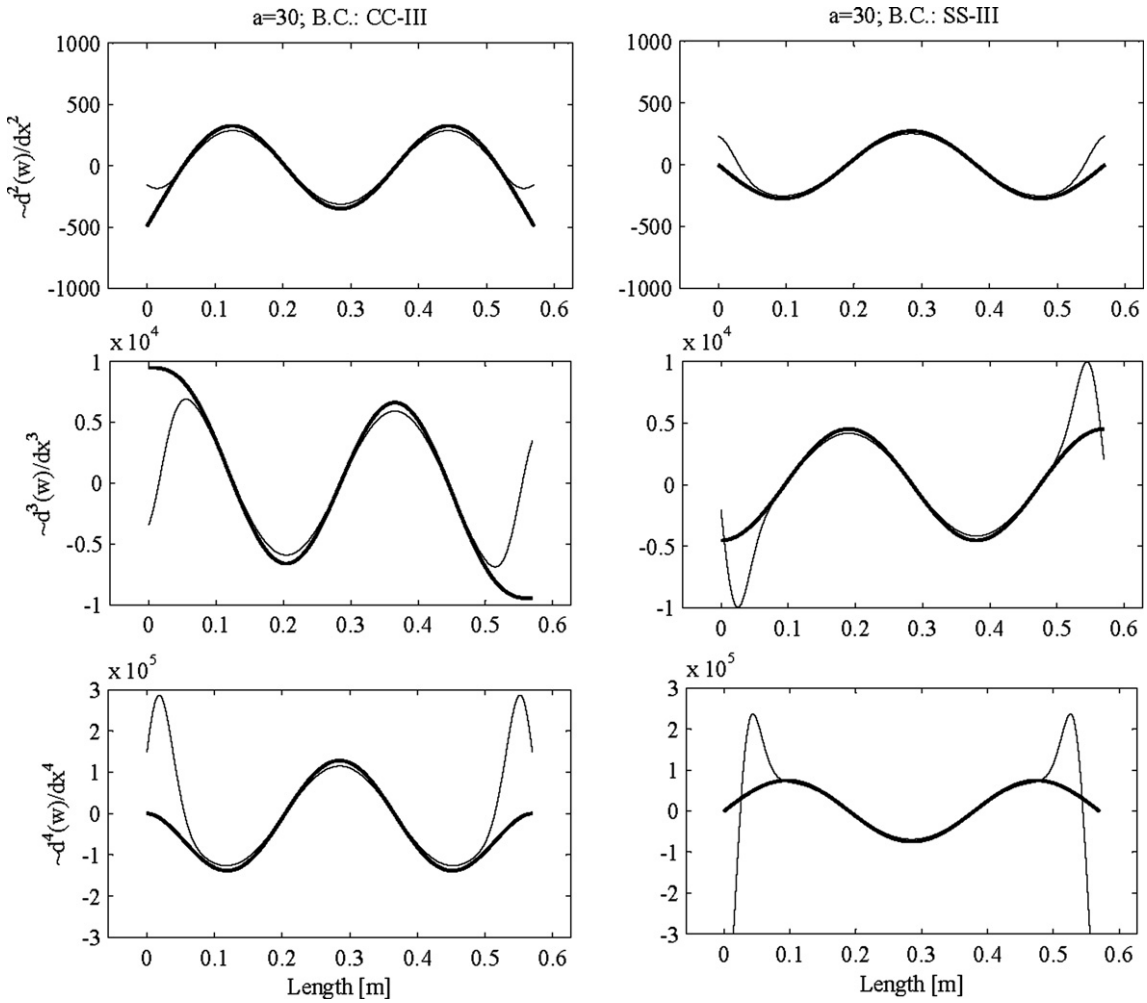

Fig. 3. Border distortion for the third mode shape of undamaged CC and SS beams (616.16 and 452.69 Hz, respectively; based on classical Euler–Bernoulli beam model); influence of the dilation parameter from the second up to the fourth derivative on mode shapes free of noise (bold line: exact derivative).

making use of derivatives beyond the second which was initially suggested by Pandey et al. (1991). This was noticed by Gentile and Messina (2002) who extended the investigation up to the third derivative and after, Rucka and Wilde (2006a,b) and Di Sante et al. (2008) identified damaged locations by also using the fourth derivative.

As is clear in Figs. 2 and 3, a different influence of the dilation parameters on mode shapes, when the modes are characterized by beams subjected to different boundary conditions, exists. It is interesting to notice how the longer the analyzing wavelet (higher a) is the more the inner points are influenced by the border distortions.

Fig. 4 illustrates the case of mode shapes contaminated by a 60 dB noise. The noise, as is known (Messina, 2004), is controlled by the magnitude of the dilation parameter and here it is confirmed that such a control is effective up to the fourth order of differentiation.

Based on the above mentioned figures, in spite of the excellent behaviour provided by the CWT for obtaining high order derivatives with controlled noise, it is clear that the advantages obtained by ponderously using dilation parameters could be paid by heavy border distortions.

Moreover, relevant limitations of CWT, in identifying damaged sites, can also exist depending on the number of measured points (Gentile and Messina, 2003; Messina, 2004). However, in this latter respect, because the objective of this manuscript is to deal with self-contained methods (i.e. basic characteristics of the CWT

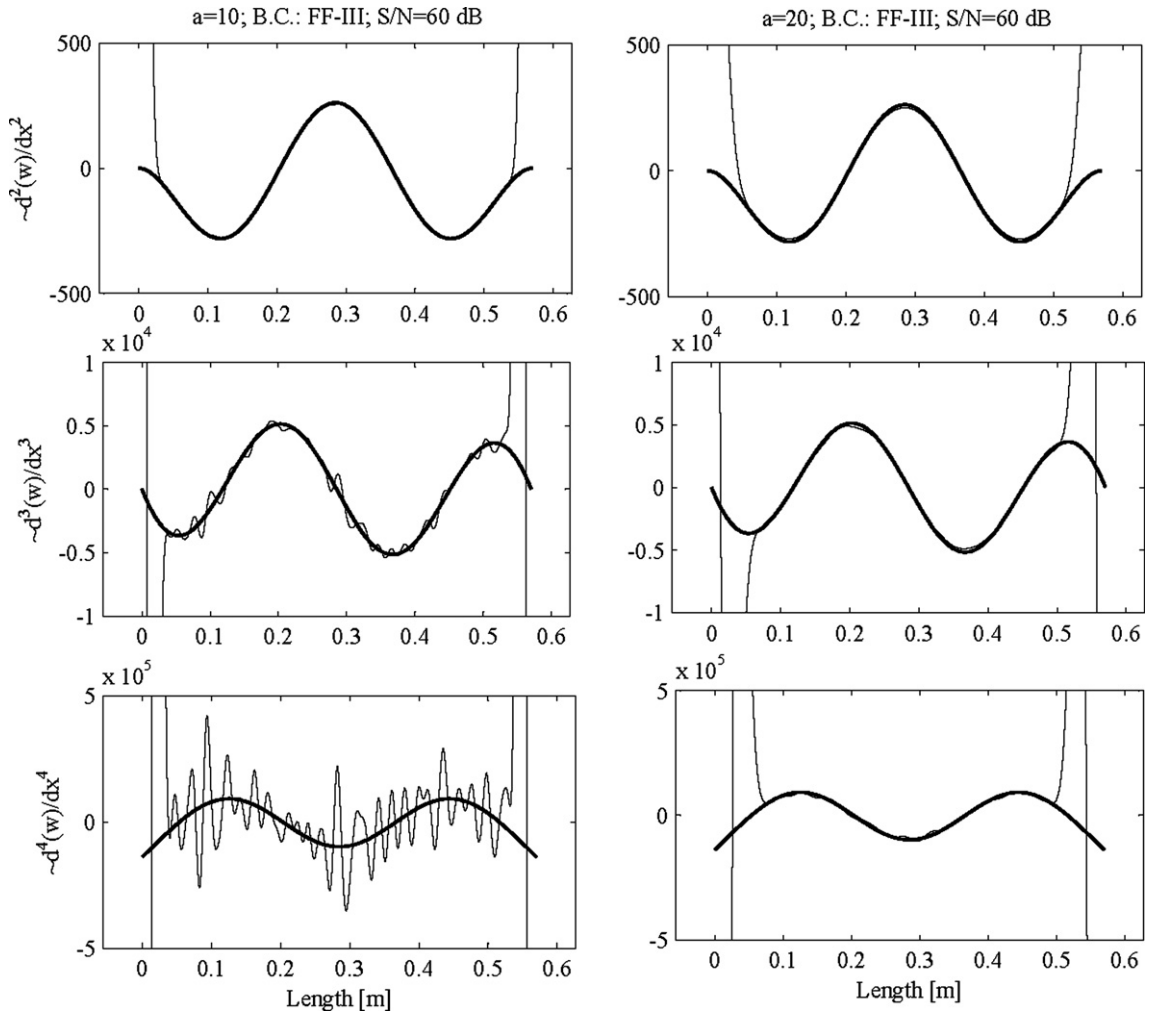

Fig. 4. Border distortion for the third mode shape of an undamaged FF beam (616.16 Hz; based on classical Euler–Bernoulli beam model); influence of the dilation parameter from the second up to the fourth derivative on mode shapes contaminated by noise ($S/N = 60$ dB; bold line: exact derivative).

are not influenced), the relevant dependence of the methods on the number of measured points belongs to the discussions already established in the past.

A method which avoids the border distortion, regardless of the dilation parameter, would evidently be worthy of interest. Indeed, such a method would leave the analysts free from ineffective partitions (whenever possible) as well as allowing straightforward numerical analysis to be carried out on relevant experimental data by simply changing the dilation parameter.

The solution to such a problem is herein attempted by resorting to the inherent significance of Eq. (1). In particular, the border distortion is evidently caused by the convolution supporting Eq. (1) along with its substantial mathematical treatment (the derivative). When the end of a finite domain is encountered the convolution estimates the changing shape and, therefore, high values of CWT can be developed. Therefore, based on these causes, a resolution of the border distortion phenomenon can be: *to extend the original signal outside its original domain*. In spite of such a mentioned simplicity (in principle), many methods effectively solving the problem cannot be counted. Rucka and Wilde (2006a,b) used an extrapolation based on spline through three or four boundary points whilst general mathematical suggestions, non immediately suitable within the present context, can be found in Strang and Nguyen (1996) and Misiti et al. (2006b). In the next sections two methods,

based on the principle of extending the original domain, are presented and compared with what currently exists in the literature. Both methods are able to work with practical measured data.

3.1. Method 1: isomorphisms

This method consists of adding an additional virtual beam to the ends of the measured points. In such a position, the method consists of adding to the left-side and to the right-side of the original data another set of data which are already available from the a-priori measuring process. The only practical disadvantage of the present method is that the original set of data will be tripled (minus two points in this work). Moreover, it is underlined that the present method needs a certain participation of the analyst as the method is ineffective when established differential orders are used respect to certain boundary conditions.

In order to present the method, let us define a finite function $f(x)$: $[a,b] \rightarrow \mathbf{R}$(Fig. 5); this function should be intended as the dynamical shape subject to be analysed because potentially containing structural information.

Based on Fig. 5, let us define *Rotation* as an isomorphism or global transformation of $f(x)$ resulting from a sequence of rigid body motions. This global transformation consists of the sequence "$g_1(x)$, $g_2(x)$, $g_3(x)$, $g_4(x)$" providing $g_4(x)$, which, constitutes a herein so-called *Rotation*; these functions are obtained by translations and out-of-plane rotations. Such a global *Rotation* can be obtained by sequentially cascading the following operations:

$$\begin{aligned} g_1(x) &= f(-x) \quad \text{out-of-plane rotation}(-180^\circ \mid y) \\ g_2(x) &= -g_1(x) \quad \text{out-of-plane rotation}(+180^\circ \mid x) \\ g_3(x) &= g_2(x-2\cdot b) \quad \text{translation}(+2\cdot b \mid x) \\ g_4(x) &= g_3(x) + 2\cdot f(b) \quad \text{translation}(+2\cdot f(b) \mid y) \end{aligned} \tag{2}$$

yielding the following explicit expression for the virtual function added to the right-side of $f(x)$:

$$g_4(x) = g_r(x) = -f(2\cdot b - x) + 2f(b); \tag{3}$$

the virtual function $g_r(x)$ has the following inherent property in $x = b$ (the number of apexes in (4) represent the order of derivation, "+" means the right derivative and "−" stays for the left derivative):

$$\begin{aligned} g_r(x) &= f(x) \\ g_r(x)'^{+} &= f(x)'^{-} \\ g_r(x)''^{+} &= -f(x)''^{-} \\ g_r(x)'''^{+} &= f(x)'''^{-} \end{aligned} \tag{4}$$

i.e. along with the continuity in $x = b$, all the odd differentiator orders are coincident, conversely all the even differentiator orders have opposite sign. This property is, therefore, assigned to the so-called *Rotation* which has been carried out in order to preserve the first derivative in $x = b$.

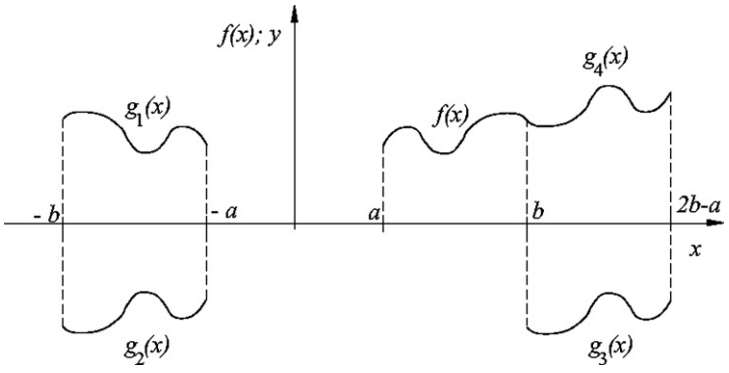

Fig. 5. Sequence (or isomorphism) of functions obtaining the *Rotation*.

Another *Rotation* of $f(x)$ can be carried out in order to join another virtual function at the left-side of the original function. This further *Rotation* leads, by carrying out similar sequences to the previously mentioned, to the following function:

$$g_4(x) = g_l(x) = -f(2 \cdot a - x) + 2f(a); \tag{5}$$

which is still characterized by an analogue set of properties (4) in $x = a$.

As far as the present context is concerned, another global transformation is considered relevant: the *Turnover*. Such a global transformation essentially consists of making a turnover of the original function around y-axis and its relevant edge ($x = a$ or b). Such a global transformation can, by referring to $x = a$, be obtained by sequentially cascading the following two operations:

$$\begin{aligned} &g_1(x) = f(-x) \quad \text{out-of-plane rotation}(-180^\circ \mid y) \\ &g_2(x) = g_1(x - 2 \cdot a) \quad \text{translation}(+2 \cdot a \mid x) \end{aligned} \tag{6}$$

which provides the following left virtual function:

$$g_2(x) = g_l(x) = f(2 \cdot a - x) \tag{7}$$

and, similarly, for the right-side:

$$g_2(x) = g_r(x) = f(2 \cdot b - x) \tag{8}$$

Eqs. (7) and (8) illustrate a dual set of properties with respect to Eqs. (4). Indeed, Eqs. (7) and (8), show how the *Turnover* at $x = a$ and b, along with the continuity of the functions, causes all the even differentiator orders to be coincident, conversely all the odd differentiator orders have opposite sign.

In conclusion, the method being dealt with in essentially consists of extending the original function with itself through two global transformation: *Rotation* and/or *Turnover*.

Before carrying out relevant numerical tests observations are worthy of note. Firstly, both the presented global transformations, *Rotation* and *Turnover*, must be considered dual for the inherent mentioned properties (i.e. (4) and its dual to (4) regarding the *Turnover*). Both the transformations can be straightforwardly obtained by a numerical point of view. For example, the extension at the right-side of an original row-set of data (i.e. the "mode") can be easily obtained by two numerical instructions (MATLAB language Ver. 7.3 (Rel.2006b)):

$$\begin{aligned} &\textit{Rotation} : \text{right\_mode} = -\textit{fliplr}(\text{mode}(1 : N - 1)) + 2 * \text{mode}(N); \\ &\textit{Turnover} : \text{right\_mode} = \textit{fliplr}(\text{mode}(1 : N - 1)); \end{aligned} \tag{9}$$

representing, Eq. (9), the numerical version of Eqs. (3) and (8). In Misiti et al. (2006b), the function "wextend" contains the *Turnover* through the 'sym' option, but the *Rotation* does not exist or at least it does not exist as in (9) even though it could be considered present only in part with the 'asym' option in the function "wextend". Finally, it should also be taken into account that the *Rotation* (9) gets two own positive characteristics: (i) a smooth extension of order 0 (function continuity) and 1 (first derivative continuity) is naturally obtained along with the continuity of all the subsequent odd order of derivative; (ii) the smooth extension of order 0 and 1 is strongly stable against data containing noise and, therefore, it should be preferred when compared to other smooth extensions based on extrapolating methods which try to estimate boundary derivatives (e.g. option 'spd' or 'sp1' in "wextend" function (Misiti et al. (2006b)), local and/or global interpolating procedures, etc.) and for which the results could be unreliable with respect to an expected smooth extension.

Numerical tests based on extensions based on *Rotation* and *Turnover* follow on specific classical (C, F, S) boundary conditions in order to investigate how much the *border distortion* phenomenon is affected by these type of extensions.

The following Figs. 6–8 illustrate cases of classical boundary conditions identical on both the edges; this choice has been taken into account for the sake of brevity but it should not be considered a limitation because both the *Rotation* and *Turnover* can be singularly applied on each edge.

In particular, Fig. 6 illustrates the case of a beam with boundary conditions CC extended by *Turnover* (T) at both the edges (the graph on the top). The left-graphs of Fig. 6 illustrate the derivatives through the scale parameter $a = 4$ (the length of the analyzing wavelet is 8% of L), whilst the right-graphs illustrate the derivatives through the scale parameter $a = 20$ (the length of the analyzing wavelet is 40% of L). Both the

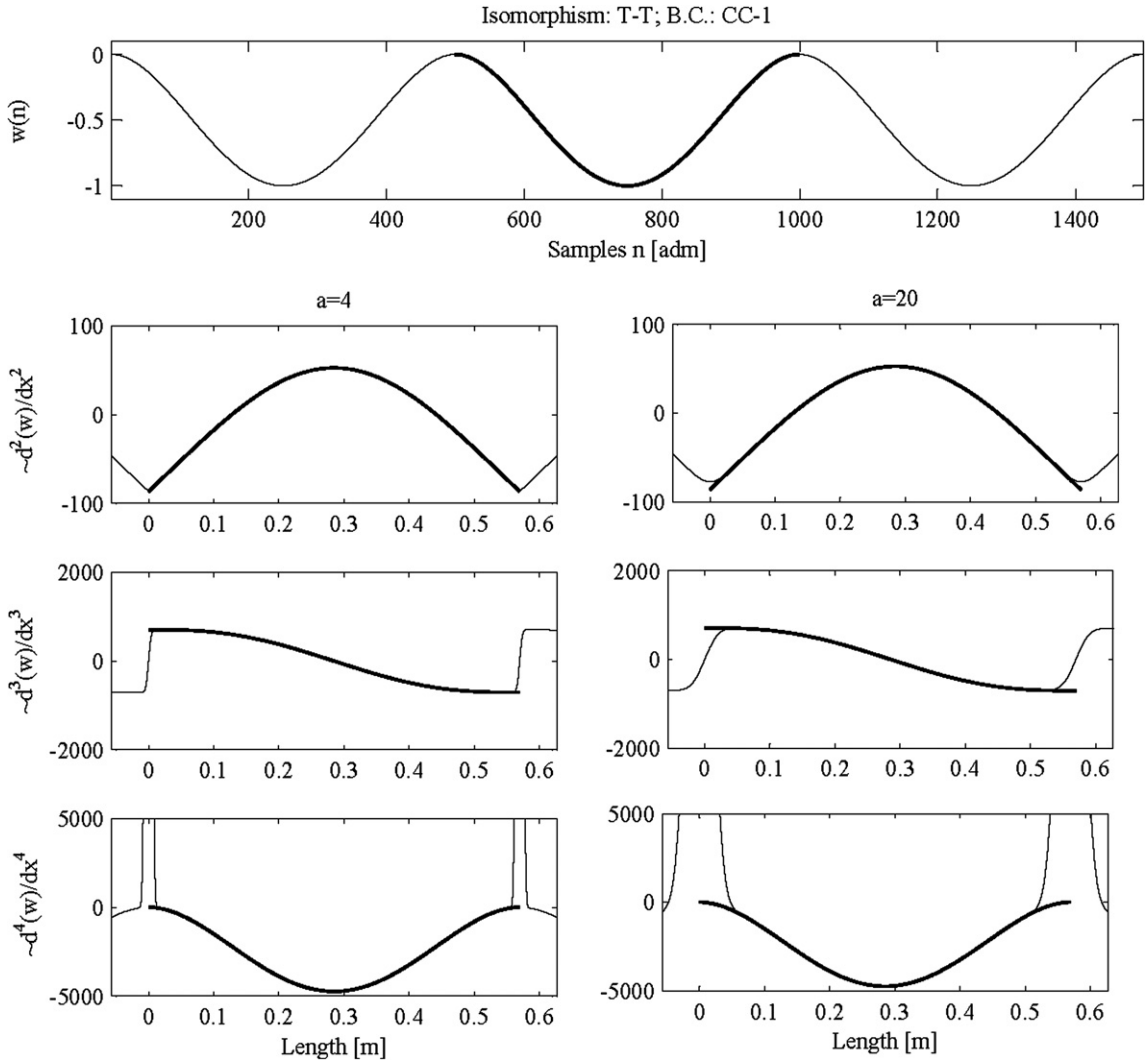

Fig. 6. Border distortion for the first mode shape of an undamaged CC beam (114.02 Hz; based on classical Euler–Bernoulli beam model); influence of *Turnover–Turnover* (Ref. Fig. 2).

mentioned graphs contain the exact derivative (bold line) overlapping the approximate one (estimated through the CWT); these latter are displayed with a thinner line. This particular case (CC) effectively is not characterized by a heavy border distortion because the edges are "quasi-smoothly" connected with the outside space; however, in spite of this fact the *Turnover* extension provides a slight benefit. Such a benefit is clearer by comparing the second derivatives between Figs. 2 and 6; however, it should also be recognized that some benefits on the *border distortion* phenomenon are also obtained for the third derivative.

It is stressed that for this particular boundary condition (CC), the continuity in $x = 0, L$ is guaranteed up to the second derivative by the geometric boundary conditions imposed at the edges: nil first derivative. Indeed, this latter condition, along with the inherent properties of the *Turnover* extension, guarantees the continuity up to the second derivative and permits a reduction of the border distortion phenomenon through a CWT based on a Gaussian 2 (i.e. second derivative). The *Rotation* extension, for the specific case of clamped edge, would provide worse results than classical CWT (Figs. 2–4). This statement can be observed in Fig. 7.

Fig. 7 is the counterpart of Fig. 3 (classical CWT). The bold line is the exact derivative, the dashed line is the classical CWT (identical to the solid thinner line of Fig. 3) and, finally, the solid thinner line is the CWT of the extended signal.

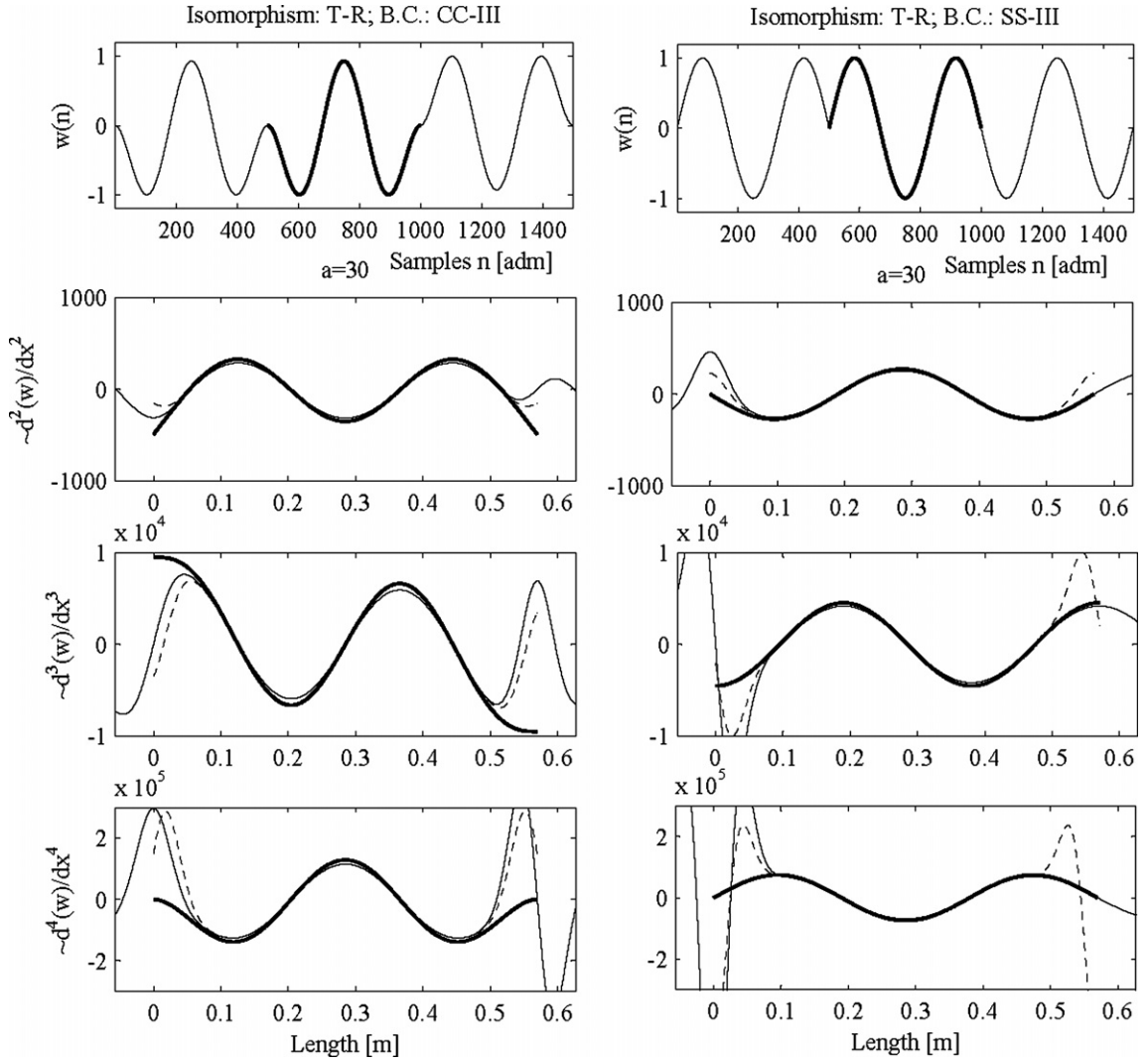

Fig. 7. Border distortion for the third mode shape of undamaged CC and SS beams (616.16 and 452.69 Hz, respectively; based on classical Euler–Bernoulli beam model); influence of *Turnover–Rotation* (Ref. Fig. 3).

In Fig. 7 the extension is not the same at the edges. Indeed, the left edge is subjected to a *Turnover* extension whilst the right edge undergoes a *Rotation* extension (top-graphs). At the left edge of the CC beam an improvement of the border distortion can be noticed; but, at the right edge of the same beam the extension (*Rotation*) provides worse results on the border distortion phenomenon on all the derivatives. This would suggest that a slight benefit, in the case of the clamped edge and even though naturally slight, can be obtained for the second derivative through the *Turnover* extension only.

The graphs in the right column of Fig. 7 illustrate an excellent reduction of the border distortion phenomenon on simply supported (SS) edges when the *Rotation* is used in the place of the *Turnover* extension. It should also be noticed, in this latter case, that the border distortion is definitely absent up to the fourth derivative. Worthy of attention is the fact that all the relevant considerations of Fig. 7 regard an analyzing wavelet having a remarkable length (60% of L).

As a conclusive test, regarding the influence of noise along with extensions, Fig. 8 is, finally, taken into account. Fig. 8 is displayed by following the identical conventions of Fig. 6. The mode shape $w(n)$ contains an amount of noise which is characterized by a $S/N = 60$ dB and, as is clear from the top-graph, *Rotation* extension has been applied on both the edges. The performance offered by the *Rotation* extension is generally

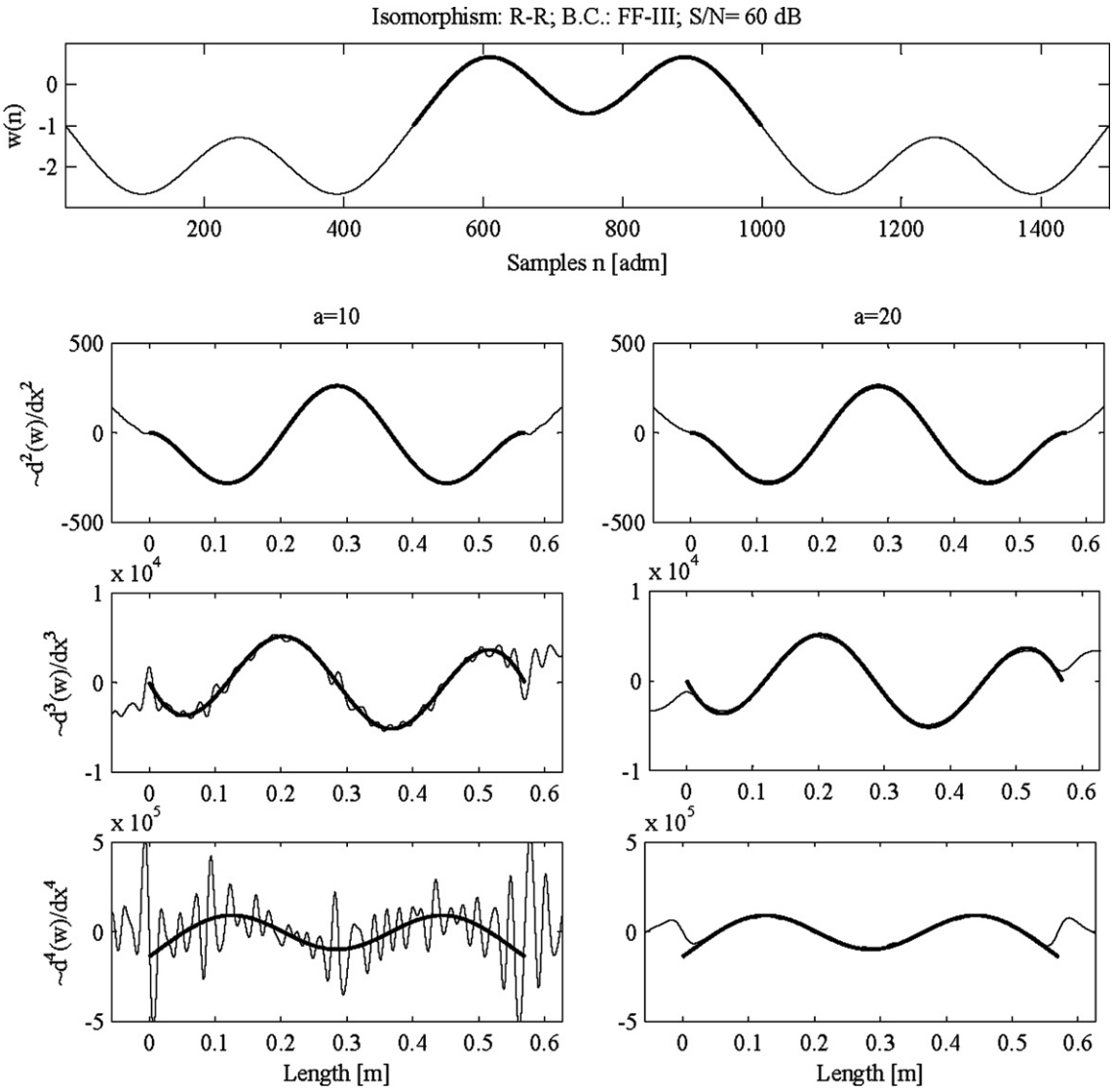

Fig. 8. Border distortion for the third mode shape of an undamaged FF beam (616.16 Hz; based on classical Euler–Bernoulli beam model); influence of *Rotation–Rotation* (Ref. Fig. 4).

excellent against noise at the edges. This can be decisively argued by also comparing Fig. 8 with its counterpart (Fig. 4).

It is clear that the stability offered at the edges by *Turnover* and *Rotation* extensions, in the presence or not of noise, is due to the fact that estimations of boundary derivative are not taken into account because the method is only based on the replicate of an original signal dependent on the particular boundary condition encountered. In this respect, the suggested method has a decisively higher performance than methods based on estimations of boundary derivatives (e.g. option 'spd' or 'sp1' in "wextend" function or extrapolating spline); this is true especially in real cases where the noise over a high number of space-sampled points could provide unreliable results in expected smooth extended data.

In order to conclude the above presented analysis, Table 1 recaps the quality of reduction of the border distortion phenomenon dependent on the particular classical boundary condition taken into account. Table 1 shows that a classical boundary condition has its own isomorphism (*Turnover* or *Rotation*) which can assist in order to tackle the border distortion.

Table 1
Boundary conditions and quality of reduction of border distortion

BC	Order (o) of derivative	*Turnover*			*Rotation*		
		Poor	Good	Excellent	Poor	Good	Excellent
C	2		•		•		
	3	•			•		
	4	•			•		
F	2	•					•
	3	•				•	
	4	•			•		
S	2	•					•
	3	•					•
	4	•					•

Based on the above presented analysis the border distortion phenomenon would seem to be completely solved through Table 1. Unfortunately this is true only in part because (i) the boundary conditions are very often uncertain in practical measurements and, finally, (ii) the measurements, in several real situations, are not exactly carried out between the edges for practical reasons and for the need to investigate only a part of the whole structure. In such cases, the above illustrated method can have inherent limitations in reducing border distortion phenomenon. In this respect, the following method (self-minimization) has been devised for tackling the above mentioned *sui generis* applications.

3.2. Method 2: self-minimization

The principle on which the present method is based still consists of extending the original data; however, the extension is not performed in only one step but in a number of adaptive steps where the first step provides an extension of the first approximation. The subsequent adapting steps have the objective of correcting the extension of the first approximation. The first step tries to extrapolate at the edges of the beam a set of data guaranteeing the continuity and tackling the border distortion phenomenon due to (1). As has been done with method 1, the subsequent discussions deal with extensions of length L.

The extension based on the first approximation can be in principle done through several extrapolating numerical methods which in nature can be global (the characteristics of the shape at the edges is estimated by taking into account the whole domain of the beam) or local (the characteristics of the shape at the edges is estimated by taking into account some points placed at the edges). What, however, should be accepted is the fact that, depending on geometries and on the amount of noise contained in the original data, the first approximation can be far from providing a smooth extension; in this case the rises occurring at the edges by (1) can be due to a non-smooth extension. Therefore, the problem is to find a method which corrects the first approximation by searching for a smoother extension at the edges. The method should also be able to work in the presence of noise with a certain robustness.

The present method aims at correcting the extension of the first approximation by minimizing an objective function which depends on the result of convolution (1). In other words, what is minimized are improper rises at the edges by trying to keep useful rises which can be an indication of real damage. In order to illustrate the present method Fig. 9 should be taken into account.

Fig. 9, sketches the original dynamical shape $w(n)$ in the samples domain between n_1 and n_2. The functions $p_l(n)$ and $p_r(n)$ are, respectively, the left and the right polynomial extending w (n) outside its original domain $[n_1, n_2]$. The polynomial discrete values placed outside domain $[n_1, n_2]$ can be assessed once function values and derivatives of $w(n)$ at the edges are known or have been estimated in some way. For example, both the above mentioned polynomials, if a third order is assumed, will have the following explicit expressions (centred in $[-1/2, 1/2]$ without losing any generality) when boundary derivatives have been predicted:

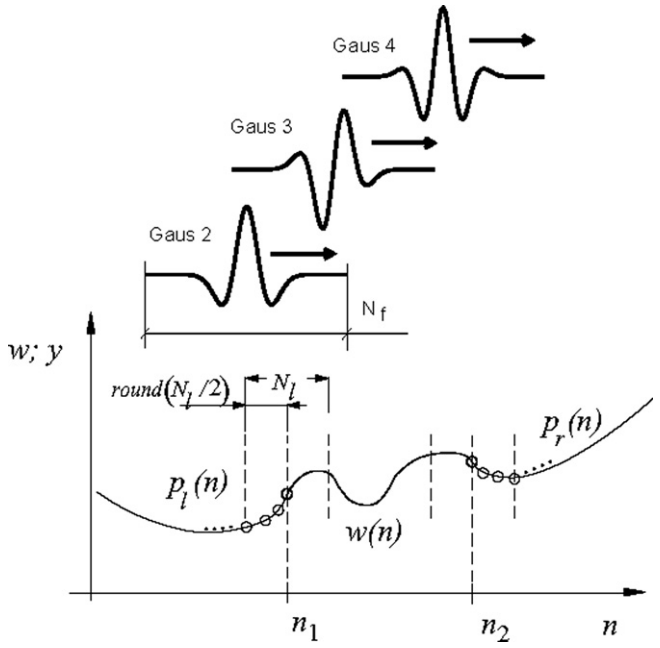

Fig. 9. Nomenclature referred to the self-minimization method.

$$p_l(c_j^l;n) = a_3n^3 + a_2n^2 + a_1n + a_0; \tag{10}$$

$$p_r(c_j^r n) = b_3n^3 + b_2n^2 + b_1n + b_0; \tag{11}$$

$$(a_3, b_3) = (c_3^l, c_3^r)\cdot y_3/6;$$

$$(a_2, b_2) = (c_2^l, c_2^r)\cdot y_2/2 \mp (c_3^l, c_3^r)\cdot y_3/4;$$

$$(a_1, b_1) = (c_1^l, c_1^r)\cdot y_1 + (c_3^l, c_3^r)\cdot y_3/8 \mp (c_2^l, c_2^r)\cdot y_2/2;$$

$$(a_0, b_0) = (c_0^l, c_0^r)\cdot y_0 \quad \mp (c_3^l, c_3^r)\cdot y_3/48 + (c_2^l, c_2^r)\cdot y_2/8 \mp (c_1^l, c_1^r)\cdot y_1/2;$$

with the imposed conditions at $n = 1/2, -1/2$; the superior and inferior sign regards the left and right polynomial, respectively, y_j ($j = 0, 1, 2, 3$) mean the values of w, first, second and third derivative, respectively, at the corresponding edges of left and right polynomials. Based on Eqs. (10) and (11) the need to resort a method for estimating derivatives at the edges (i.e. y_1, y_2, y_3) is clear. Due to the natural difficulty of making such an estimation, $p_l(n)$ and $p_r(n)$ should be considered as a first approximation at the first step (when the non-dimensional coefficients (c_j^l, c_j^r for $j = 0$, 1, 2, 3 are settled to 1); on the other hand, the corrective coefficients should be accordingly changed in order to accommodate an effective smooth extension up to the requested order.

In the presence of noise, for general shapes and different boundary conditions, the estimation of the derivatives is even more difficult. In this work, a global method has been chosen in order to evaluate the first approximation for the derivatives of $p_l(n)$ and $p_r(n)$ at the boundaries. The mentioned global method essentially consists of estimating the derivatives through polynomials which globally fit the original data; this is done through curve fitters available in MATLAB Ver. 7.3 (Rel.2006b) along with the tact of centring and scaling the abscissa values (the degree of global polynomial fitting could be thus chosen also very high without substantially noticing ill conditioning problems).

Once both left and right polynomials ($p_l(n)$,$p_r(n)$) are established as the first approximation and are joined to the original set of data, the minimization process can be finally performed. In order to show such minimization procedure, which, constitutes the core of the method, Fig. 9 should be again taken into consideration along with the following points:

(i) the border distortion phenomenon involves a larger domain of interest when higher scales are used; (ii) as far as the length influenced by border distortion phenomenon is concerned, it is approximately 1/2 the length of the analyzing wavelet (neglecting a certain influence coming from the order of the Gaussian wavelet); (iii) a couple of local polynomials $(p_l(n), p_r(n))$ having smoother extensions at the boundaries than the first approximation should exist; (iv) the rises due to border distortion phenomenon occur close to boundaries at both inner and outer points (e.g. Figs. 2–4 and 6–8).

Therefore, based on the above mentioned points (i–iv), if the first approximation is not retained sufficient, the border distortion phenomenon is tackled by solving the following problem:

$$\begin{cases} \min\limits_{c} F(c_j^l, c_j^r) \\ \qquad \text{subject to} \\ -10^5 \leqslant c_j^l \leqslant 10^5 \quad \forall j \\ -10^5 \leqslant c_j^r \leqslant 10^5 \quad \forall j \end{cases} \tag{12}$$

where the objective function F in (12), with the nomenclature referred to Fig. 9, has expression (13).

In (13) any fraction of integer number is intended numerically rounded to its nearest integer. Eqs. (12) and (13) show a minimization procedure which looks for a set of non-dimensional coefficients $c_j^{l,r}$ with $j = 0, 1, 2, 3$ having the initial guess point settled at 1 for any j.

$$\begin{cases} F(c_j^l, c_j^r) = \left(\begin{array}{l} \left\| \sum\limits_{i=N-N_l^e-1}^{N} [D_o(w_e(n_i); a) - D_o(w_e(N/2); a)] \right\| \\ + \left\| \sum\limits_{i=2\cdot N-1}^{2\cdot N+N_r^e} [D_o(w_e(n_i); a) - D_o(w_e(2\cdot N + N/2 - 1); a)] \right\| \end{array} \right) \Big/ \left\| \sum\limits_{i=N+N_l^i}^{2\cdot N-1-N_r^i} D_o(w(n_i); a) \right\| \\ w_e(n_{i,j,k}) = [p_l(n_i) \cup w(n_j) \cup p_r(n_k)] \\ \qquad\qquad i = 0, \ldots, N-2; \\ \qquad\qquad j = N-1, \ldots, 2\cdot N - 1; \\ \qquad\qquad k = 2\cdot N, \ldots, 3\cdot N - 2; \\ p_l(c_j^l; n) = a_3(c_j^l) n^3 + a_2(c_j^l) n^2 + a_1(c_j^l) n^1 + a_0(c_j^l) \\ p_r(c_j^r; n) = b_3(c_j^r) n^3 + b_2(c_j^r) n^2 + b_1(c_j^r) n^1 + b_0(c_j^r) \end{cases} \tag{13}$$

Based on Eqs. (10) and (11) these coefficients have an immediate interpretation because they are non-dimensional and multiply the derivative and the function values assumed at the borders; for example, the value "1" corresponds to accept the first approximation, whilst the value zero can settle established nil boundary conditions. It should also be noticed that the value function can be corrected due to the fact that it is established by the fitting polynomials.

In such a statement of the problem (12) and (13) the order of the differentiation, o in Eq. (1), must be coincident with the order of the polynomial (i.e. third order if $o = 3$). This coincidence is due to the need to satisfy the principle on which the objective function (13) is based. In particular, if D_o corresponds to D_3, Eq. (1) provides the third derivative and, therefore, being the extrapolating polynomial $(p_l(n), p_r(n))$ of third order, the result of Eq. (1) is constant at a convenient distance from the borders (~middle of the outside domains $[(0, N-2)$ and $(2N, 3N-2)]$). These constant values are subtracted from the rises immediately outside the beam and here assumed as $N_l^e = N_r^e \approx N_f/4$ (sum of differential rises are so obtained and placed at numerator of (13)). Moreover, in (13) the differential rises are referred to the norm of CWT regarding the inner central points in $[n_1, n_2]$; in this respect the points immediately inner and close to the boundaries $(N_l^i = N_r^i \approx N_f/3)$ are excluded in order to avoid comparisons with unstable values due to border distortions. Numerator and denominator of Eq. (13) can finally be compared to the relevant number of points present in the domain of interest in order to minimize a ratio of densities as has been done in the following numerical evaluations.

In conclusion, Eqs. (12) and (13) correct the polynomials of the first approximation by minimizing the rises of D_o immediately outside $[n_1, n_2]$ with respect to the constant derivative placed within the extensions but far away from the boundaries.

Based on this latter principle, Eqs. (12) and (13) offer substantially two different choices: (i) the order of differentiation (o) in Eqs. (12), (13) and (1) can be 2, 3 or even 4, but, in such eventuality left and right polynomials ($p_l(n), p_r(n)$) must be second, third and fourth degree, respectively (Eqs. (10) and (11) must be accordingly re-adapted in the cases); (ii) Eqs. (12) and (13) can be based on an established order of differentiation (for example: $D_o = D_4$) in order to tackle the border distortion phenomenon at the boundaries and, lower order of differentiation (as for the example: $D_o = D_3$ or D_2) can be assessed by Eq. (1). This latter choice is supported by the fact that if a high order differentiation is enforced to be continuous there is ground for expecting continuity at lower order of differentiations (therefore, reductions of the border distortion phenomenon). Numerical comparisons, based on the evaluation of D_o through (1), have shown how the latter choice (ii) is more accurate than the former (i).

In spite of the different choices offered by the above illustrated method, the higher sensitivity of higher order differentiations on the noise naturally contained in the measurements and, therefore, the need to use larger scales must also be considered. This can limit the choice to work with unconditionally high differentiator orders. In conclusion, the combination to work with D_3 in (12) and (13) and evaluate D_2 through (1) or to work with D_4 in (12) and (13) and evaluate D_3 and D_2 through (1) has been retained an acceptable choice for showing the performance of the method as can be seen in the next sections.

4. CWT and self-minimization on undamaged beams

In this section, a number of simulations showing the performance of the self-minimization method, aimed at reducing the border distortion phenomenon, are shown. The simulations regard undamaged beam in order to illustrate both the capability of the method to contain the performance of the method based on isomorphism and to show the stability of the method to perform well compared to basic shapes. Finally, the several simulations carried out will also be able to illustrate the fundamental potentiality of the method.

Table 2 illustrates the results of a number of simulations where D_3 has been used to carry out the minimization whilst Eq. (1) has been used to estimate the second derivative; the performance of the method can be seen by looking at the 10th column where the maximum error committed on the second derivative is provided. The maximum error is evaluated by taking into account the maximum of a point by point error evaluation which in this work is always assessed through Eq. (14) (when the exact derivative is available).

$$\text{Error}[\%] = \left| \frac{\mathrm{d}^o w}{\mathrm{d}x^o}_{\text{estimated}} - \frac{\mathrm{d}^o w}{\mathrm{d}x^o}_{\text{exact}} \right| \cdot 100 \Bigg/ \left| \frac{\mathrm{d}^o w^{\text{Max}}}{\mathrm{d}x^o}_{\text{exact}} - \frac{\mathrm{d}^o w^{\text{Min}}}{\mathrm{d}x^o}_{\text{exact}} \right| \tag{14}$$

This 10th column shows two numbers; those in parenthesis regard the error committed by the estimation (CWT_2) without correcting the first approximation through the self-minimization.

Table 2
Performance method 2 on CC-I beam (noise free); bounded; minimization based on D_3

a (o_l, o_r)	$p_l(n)$				$p_r(n)$				Max Error[a] [%]	CPU time [s]
	c_0	c_1	c_2	c_3	c_0	c_1	c_2	c_3		
4 (5,5)	0.0000	0.0000	0.7953	0.6295	0.0000	0.0000	0.7953	0.6294	0.02(204)	55
20 (5,5)	0.0000	−0.0002	0.7951	0.6282	−0.0001	−0.0003	0.7951	0.6281	0.44(22.2)	48
30 (5,5)	−0.0005	−0.0017	0.7942	0.6250	−0.0005	−0.0017	0.7942	0.6250	0.99(18.9)	36
50 (5,5)	−0.0088	−0.0185	0.7879	0.6110	−0.0089	−0.0186	0.7879	0.6109	2.71(17.6)	25
4 (10,10)	0.9988	1.0003	0.9999	1.0001	0.9990	1.0017	0.9999	1.0001	0.18(0.18)	19
20 (10,10)	1.0000	1.0000	0.9999	0.9993	1.0000	1.0000	0.9999	0.9993	0.44(0.44)	9
30 (10,10)	1.0000	1.0000	0.9997	0.9972	1.0000	1.0000	0.9997	0.9972	0.99(0.99)	9
50 (10,10)	1.0000	1.0000	0.9979	0.9872	1.0000	1.0000	0.9979	0.9872	2.71(2.71)	10

[a] Estimation of second derivative through scale equal to a.

The first column of Table 2 illustrates the scales used in the several simulations. In the first column, the order of the global polynomials aimed at fitting modes are also indicated. These fitting polynomials provide values and derivatives for the left and right polynomials in the first approximation (10) and (11). The first four rows of Table 2 regard polynomial fitters of fifth order whilst the remaining four lines concern polynomial fitters of 10th order. Table 2 also lists the corrective coefficients (10) and (11) corresponding to the final optimum solution. Finally, the last column reports the CPU time in seconds needed by a laptop equipped with a "Pentium 4" processor and O.S. Windows XP/512MB-RAM to achieve the solution. The following tables, apart from a few clear changes, will be presented with the same conventions.

Table 2 concerns the first mode of a CC beam whose relevant boundary conditions in the classical-beam theory are value and first derivative nil.

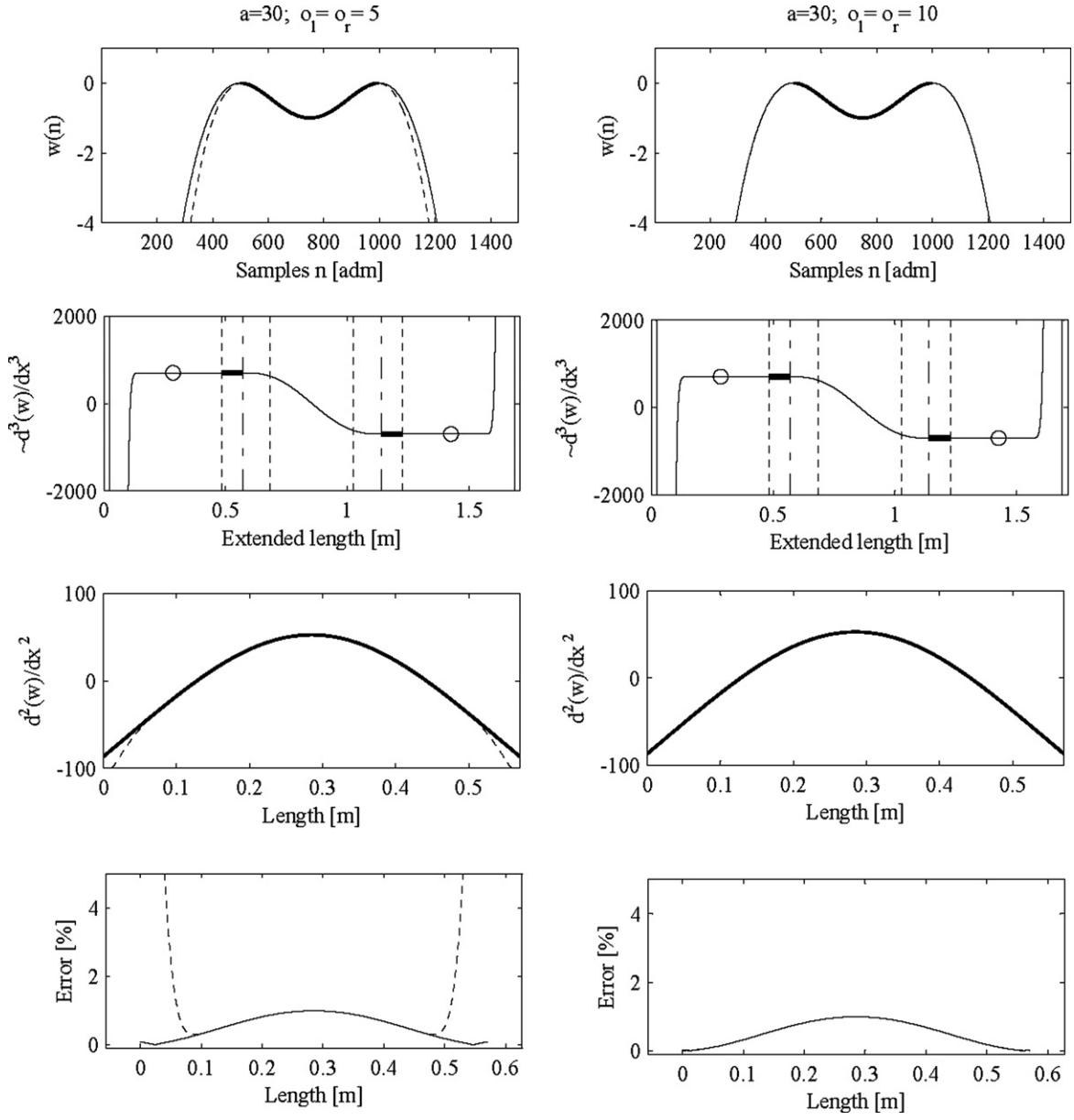

Fig. 10. Performance of self-minimization with $a = 30$ and $o_l = o_r = 10$ (ref. Table 2). Noise free.

Table 2 evidently shows that the estimation of the second derivative, through a $CWT_2(1)$ along with the self-minimization, is superior or equal to the same evaluation based on the first approximation. It is interesting to notice that an extension based on the first approximation can provide extremely high errors (204%, 22%, 19%) compared to the extremely low errors obtainable through the self-minimization (0.02%, 0.44%, 0.99%).

Table 2 also shows that the minimization algorithm achieves the solution faster when the global polynomial fitters are of 10th order (~10 s in cases of practical interest: $a \sim 20, 30$); this happens because the guess point (first approximation) is closer to the optimum solution. Indeed, the relevant coefficients regarding both the

Table 3
Performance method 2 on CC-I beam (noise free); unbounded; minimization based on D_3

a (o_l, o_r)	$p_l(n)$				$p_r(n)$				Max Error[a] [%]	CPU time [s]
	c_0	c_1	c_2	c_3	c_0	c_1	c_2	c_3		
4 (5,5)	0.0000	0.0000	0.7953	0.6294	0.0000	0.0000	0.7953	0.6293	0.02(204)	78
20 (5,5)	−0.0001	−0.0004	0.7950	0.6278	−0.0001	−0.0003	0.7950	0.6280	0.44(22.2)	54
30 (5,5)	−0.0004	−0.0015	0.7943	0.6254	−0.0007	−0.0021	0.7940	0.6246	0.99(18.9)	56
50 (5,5)	−0.0085	−0.0181	0.7881	0.6112	−0.0092	−0.0190	0.7878	0.6107	2.71(17.6)	43
4 (10,10)	1.0000	1.0000	0.9999	1.0000	1.0000	1.0000	0.9999	1.0000	0.18(0.18)	8
20 (10,10)	1.0000	1.0000	0.9999	0.9993	1.0000	1.0000	0.9999	0.9993	0.44(0.44)	14
30 (10,10)	1.0000	1.0000	0.9997	0.9972	1.0000	1.0000	0.9997	0.9972	0.99(0.99)	15
50 (10,10)	1.0000	1.0000	0.9979	0.9872	1.0000	1.0000	0.9979	0.9872	2.71(2.71)	14

[a] Estimation of second derivative through scale equal to a.

Table 4
Performance method 2 on CC-I beam (noise free); bounded with $c_0 = c_1 = 0$; minimization based on D_3

a (o_l, o_r)	$p_l(n)$				$p_r(n)$				Max Error[a] [%]	CPU time [s]
	c_0	c_1	c_2	c_3	c_0	c_1	c_2	c_3		
4 (5,5)	0.00	0.00	0.7953	0.6296	0.00	0.00	0.7953	0.6296	0.02(8.39)	23
20 (5,5)	0.00	0.00	0.7953	0.6290	0.00	0.00	0.7953	0.6290	0.44(9.93)	21
30 (5,5)	0.00	0.00	0.7951	0.6277	0.00	0.00	0.7951	0.6277	0.99(10.9)	18
50 (5,5)	0.00	0.00	0.7936	0.6213	0.00	0.00	0.7936	0.6213	2.71(12.5)	15
4 (10,10)	0.00	0.00	1.0000	1.0003	0.00	0.00	1.0000	1.0004	0.02(0.02)	25
20 (10,10)	0.00	0.00	1.0000	0.9994	0.00	0.00	1.0000	0.9994	0.44(0.44)	9
30 (10,10)	0.00	0.00	0.9997	0.9973	0.00	0.00	0.9997	0.9973	0.99(0.99)	19
50 (10,10)	0.00	0.00	0.9979	0.9873	0.00	0.00	0.9979	0.9873	2.71(2.71)	9

[a] Estimation of second derivative through scale equal to a.

Table 5
Performance method 2 on CC-I beam; $o_l = o_r = 10$; bounded; minimization based on D_3

a, a_2	$p_l(n)$				$p_r(n)$				Max Error[a] [%]	CPU time [s]
	c_0	c_1	c_2	c_3	c_0	c_1	c_2	c_3		
$S/N = 40$ dB										
20	1.4629	5.6845	0.5709	6.3983	2.0100	2.7863	−2.1034	2.1118	112(44.6)	31
30	2.4229	−10.1230	1.3633	−4.2013	0.9905	1.0768	1.2494	0.2254	32.9(48.8)	37
50	0.4220	1.0158	1.1089	−2.5736	−0.0546	−0.0070	2.5963	−0.2593	3.15(60.5)	35
50, 20	=	=	=	=	=	=	=	=	6.90(44.6)	33
$S/N = 60$ dB										
20	1.8787	1.1663	0.9801	0.8807	2.0119	2.7893	0.8749	0.2729	11.2(4.46)	22
30	0.8884	0.9776	1.0019	1.0971	1.0241	1.1125	1.0078	1.4869	3.42(4.88)	18
50	0.7310	0.9843	1.0073	1.1383	0.1917	0.1949	1.0553	1.7705	2.65(6.06)	36
50, 20	=	=	=	=	=	=	=	=	1.05(4.46)	37

[a] Estimation of second derivative.

extending polynomials are ~1 when the 10th order is used, whilst, when the fifth order is taken into account the coefficients undergo a more remarkable change. In this latter respect the first two coefficients (c_0, c_1) should be taken into account: the minimization algorithm makes these coefficients close to zero consistent with the boundary conditions of a CC beam.

Table 2 cannot graphically show an interesting feature: the maximum error never occurred at the border within the domain of interest. Therefore, the border distortion phenomenon was correctly tackled by the self-minimization method. In this regard, Fig. 10 illustrates two cases numerically described in Table 2 and from which the total absence of border distortion phenomenon can be observed. Fig. 10 illustrates these two simulations by arranging the relevant cases in two different columns. In particular, by mentioning the graphs of Fig. 10 as elements in a two-dimensional matrix, graphs $10_{(1,1),(1,2)}$ illustrate mode shapes extended at left and right by $p_l(n)$ and $p_r(n)$, respectively. The solid thin lines correspond to the polynomials corrected as

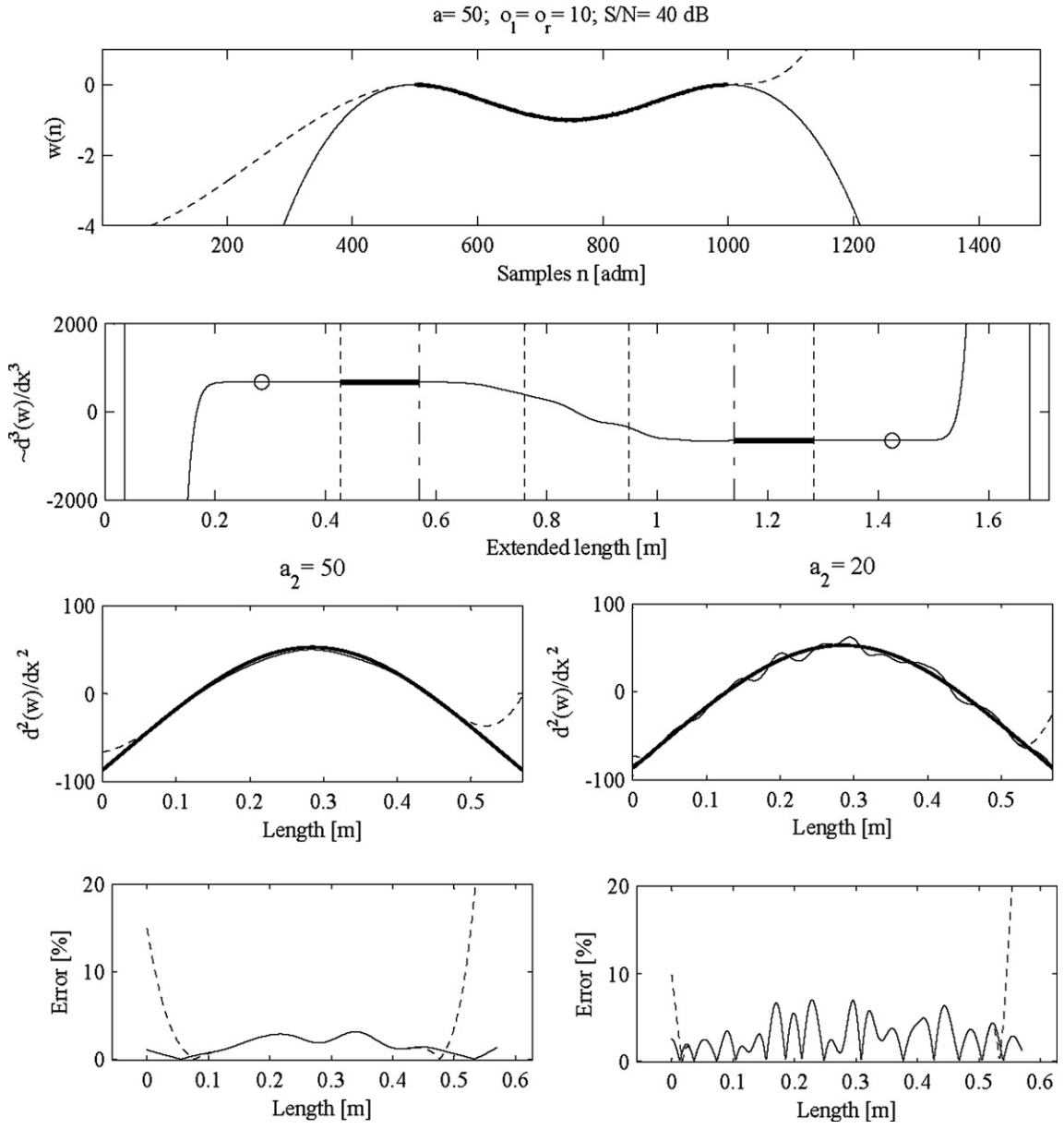

Fig. 11. Performance of self-minimization with $(a = a_2 = 50)$, $(a = 50;\ a_2 = 20)$ and $o_l = o_r = 10$ (Ref. Table 5). Noise: $S/N = 40$ dB.

achieved at the optimum solution, whilst, the dashed lines are the left and right polynomials evaluated on the basis of the values of the first approximation.

Graphs $10_{(4,1),(4,2)}$ illustrate the point by point percentage errors (14) without minimization (dashed line) and with minimization (solid line). Graphs $10_{(3,1),(3,2)}$ illustrate exact evaluations (thicker lines) estimations without minimization (dashed lines) and, finally estimations with minimization (solid line) of the second derivative.

Graphs $10_{(2,1),(2,2)}$ illustrate the third derivative working through Eqs. (12) and (13) in its achieved final optimum solution. In these graphs, the dot-dash lines delimit the true length of the beam whilst the dashed line delimits the domains regarding $N_l^i = N_r^i \approx N_f/3$ (inner points) and $N_l^e = N_r^e \approx N_f/4$ (outer points). In particular, the outer points are illustrated through thick lines which, along with the circles shown in graphs $10_{(2,1),\ (2,2)}$, regard the points on which the differential rises are evaluated in (13).

Fig. 10 clearly shows the ability of the self-minimization method to eliminate the border distortion. Fig. 10 also shows how a visually judicable good fit (dashed line in graph $10_{(1,1)}$) is unreliable for reducing border distortion (graph $10_{(4,1)}$). This latter statement can become even worse in the presence of noise as will become more evident in what follows.

Table 3 illustrates a set of simulations identical to those of Table 2 with an unique difference: the algorithm used in finding the optimum solution is based on unbounded variables or, as it is commonly said, the algorithm is based on an unconstrained formulation (Gill et al., 1995; The MathWorks, 2006b). It is interesting to notice, by comparing Tables 2 and 3, the robustness of the objective function (13) for reducing the border distortion phenomenon regardless of the algorithm used. In particular, it should be noticed that identical solutions were found. However, apart from the mentioned robustness, the unconstrained formulation provides a slightly slower performance for obtaining the optimum solution aimed at reducing the border distortion and, finally, does not allow the introduction of ad hoc constraints on the involved variables (c_j): for example settling part of the variables at zero, or at an established value, in the case of known boundary conditions. In this latter respect, Table 4 is of interest.

Table 4 illustrates a set of simulations identical to those of Table 2 with a unique difference: the first two coefficients (c_0, c_1) are settled (constrained) to zero. In such a situation, the velocity of the algorithm is higher even in the case where a global curve fitter of order five is used; in passing, the excellent respective symmetry among the corrective coefficients is worth mentioning; this is evidently caused by the symmetric boundary conditions (i.e. CC) along with the symmetry of the analyzed dynamical shape. Based on the mentioned reasons all the following tests regard constrained formulations.

Table 5 illustrates the performances of the self-minimization method in the presence of noise (two cases: $S/N = 40$ and 60 dB). The 10th column shows the excellent behaviour of method 2 in reducing the border distortion phenomenon especially when it is complemented with its graphical counterpart (Fig. 11). In particular, Table 5 illustrates two cases where the minimization provides worse results than the first approximation (112(44.6), 11.2(4.46)). For this the formulation (12) and (13) should not be blamed. Indeed, both the cases

Table 6
Performance method 2 on CC-I beam; $o_l = o_r = 14$; bounded; minimization based on D_3

a, a_2	$p_l(n)$				$p_r(n)$				Max Error[a] [%]	CPU time [s]
	c_0	c_1	c_2	c_3	c_0	c_1	c_2	c_3		
$S/N = 40$ dB										
20	3.1928	0.2839	−0.5746	0.0724	0.5937	0.4496	0.1373	0.0808	112(578)	26
30	5.2807	−0.5059	−1.3708	−0.0475	0.2924	0.1737	−0.0817	0.0086	32.9(710)	34
50	0.8845	0.0503	−1.1158	−0.0292	−0.0133	−0.0003	−0.1694	−0.0099	3.15(1000)	37
50, 20	=	=	=	=	=	=	=	=	7.00(578)	37
$S/N = 60$ dB										
20	3.1798	0.2879	1.1704	−0.2762	0.5947	0.4505	2.5357	−0.0178	11.2(57.8)	30
30	0.9462	0.1926	1.2106	−0.3856	0.2973	0.1771	2.9232	−0.0972	3.38(71.1)	30
50	0.9436	0.1122	1.2240	−0.4095	0.0584	0.0320	3.0580	−0.1154	2.65(100)	42
50, 20	=	=	=	=	=	=	=	=	1.10(57.8)	42

[a] Estimation of second derivative.

occurred with the scale $a = 20$ which is not sufficiently high to reduce the noise and provide an extended derivative which is smooth enough at the ends. In such circumstances, the shape is too corrupted by noise to allow the algorithm to find a smooth extension; therefore higher scales must assist the algorithm in smoothing the ends, as is, indeed, the case with $a = 30$, 50. Once the smooth extension is carried out through the minimization (12) and (13) any scale can be used to detect the damage through (1); the fourth cases in Table 5, indeed, minimize through D_3 based on scale $a = 50$ and assess the second derivative (D_2) through scale $a_2 = 20$. Both these simulations, based on $S/N = 40$ dB, are illustrated in Fig. 11 where the border distortion phenomenon is highly controlled by the minimization. The convention regarding lines is identically referred to Fig. 10.

Table 6 illustrates a set of simulations identical to those of Table 5 with a unique difference: the global polynomial curve fitter, providing the estimation of the first approximation, is of 14 rather than 10th order. As is clear from Table 6, a higher order for the global polynomial curve fitter is not a sufficient condition to ensure a

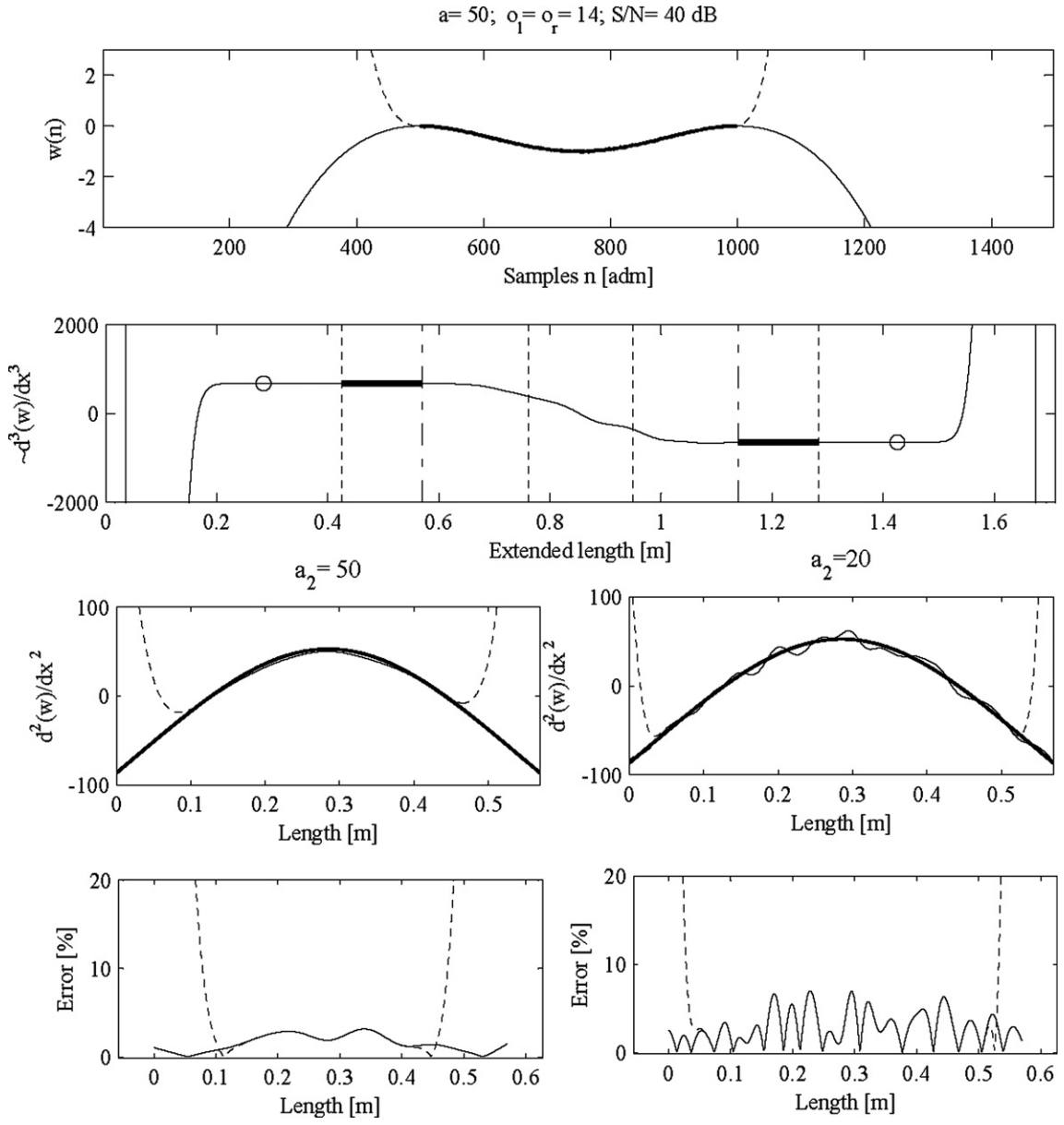

Fig. 12. Performance of self-minimization with ($a = a_2 = 50$), ($a = 50$; $a_2 = 20$) and $o_l = o_r =$ 14 (ref. Table 6). Noise: $S/N = 40$ dB.

better smoothing extension. Indeed, the first approximation provides rises at the borders containing percentage errors of several hundreds (higher than the case corresponding to use the 10th order in Table 5). However, the self-minimization, regardless of the first approximation estimations, always converges at the identical "smooth" solution obtained in the case of 10th order as can be seen by comparing the 10th columns of Tables 5 and 6. Fig. 12, basing on the same graphical nomenclature of Fig. 11, shows the performance relative to the self-minimization method for two cases of Table 6 (Max Error [%] = 3.15(1000), 7.00(578)). Fig. 12 still shows the ability of the self-minimization to remove the border distortion phenomenon and even move the maximum error far away from the borders.

Table 7
Performance method 2 on CC-I beam; $o_l = o_r = 10$; bounded with $c_0 = c_1 = 0$; minimization based on D_3

a, a_2	$p_l(n)$				$p_r(n)$				Max Error[a] [%]	CPU time [s]
	c_0	c_1	c_2	c_3	c_0	c_1	c_2	c_3		
$S/N = 40$ dB										
20	0.00	0.00	1.0639	−3.0462	0.00	0.00	3.3716	−1.0178	16.5(34.7)	12
30	0.00	0.00	1.1089	−2.5336	0.00	0.00	2.7050	−0.3497	3.57(40.2)	13
50	0.00	0.00	1.1407	−2.8051	0.00	0.00	2.5953	−0.2601	3.15(56.6)	19
50, 20	=	=	=	=	=	=	=	=	7.01(34.7)	19
$S/N = 60$ dB										
20	0.00	0.00	1.0057	1.1741	0.00	0.00	1.0953	2.3112	1.65(3.47)	10
30	0.00	0.00	1.0095	1.1497	0.00	0.00	1.0683	1.8733	1.18(4.22)	13
50	0.00	0.00	1.0107	1.1509	0.00	0.00	1.0621	1.7983	2.65(5.62)	16
50, 20	=	=	=	=	=	=	=	=	1.07(3.47)	16

[a] Estimation of second derivative.

Table 8
Performance method 2 on FF-III beam (noise free); bounded; minimization based on D_3

a (o_l, o_r)	$p_l(n)$				$p_r(n)$				Max Error[a] [%]	CPU time [s]
	c_0	c_1	c_2	c_3	c_0	c_1	c_2	c_3		
4 (5, 5)	0.6764	0.3873	−0.0016	−0.1010	0.6764	0.3873	−0.0018	−0.1066	0.25(2615)	55
20 (5, 5)	0.6763	0.3852	−0.0284	−0.3932	0.6763	0.3852	−0.0284	−0.3932	4.06(237)	34
30 (5, 5)	0.6760	0.3827	−0.0460	−0.4803	0.6760	0.3827	−0.0460	−0.4803	6.57(179)	34
50 (5, 5)	0.6769	0.3857	−0.0373	−0.4651	0.6769	0.3857	−0.0373	−0.4651	12.8(152)	30
4 (10, 10)	1.0008	1.0125	0.0443	0.2458	1.0008	1.0125	0.0443	0.2457	0.26(10.3)	49
20 (10, 10)	1.0006	1.0071	0.6822	0.8921	1.0006	1.0072	0.6815	0.8918	4.06(5.99)	19
30 (10, 10)	1.0001	1.0005	1.1035	1.0895	1.0001	1.0005	1.1034	1.0895	6.57(5.85)	21
50 (10, 10)	1.0015	1.0084	0.8953	1.0552	1.0015	1.0083	0.8956	1.0553	12.8(12.8)	21

[a] Estimation of second derivative through scale equal to a.

Table 9
Performance method 2 on FF-III beam (noise free); bounded with $c_2 = c_3 = 0$; minimization based on D_3

a (o_l, o_r)	$p_l(n)$				$p_r(n)$				Max Error[a] [%]	CPU time [s]
	c_0	c_1	c_2	c_3	c_0	c_1	c_2	c_3		
4 (5, 5)	0.6764	0.3873	0.00	0.00	0.6764	0.3873	0.00	0.00	0.11(2581)	28
20 (5, 5)	0.6735	0.3828	0.00	0.00	0.6735	0.3828	0.00	0.00	2.31(188)	17
30 (5, 5)	0.6634	0.3732	0.00	0.00	0.6634	0.3732	0.00	0.00	5.05(113)	11
50 (5, 5)	0.5995	0.3336	0.00	0.00	0.5995	0.3336	0.00	0.00	12.8(67.0)	4
4 (10, 10)	1.0008	1.0125	0.00	0.00	1.0008	1.0125	0.00	0.00	0.11(7.75)	17
20 (10, 10)	0.9965	1.0008	0.00	0.00	0.9965	1.0008	0.00	0.00	2.31(2.31)	7
30 (10, 10)	0.9815	0.9756	0.00	0.00	0.9815	0.9756	0.00	0.00	5.05(5.05)	8
50 (10, 10)	0.8870	0.8722	0.00	0.00	0.8870	0.8722	0.00	0.00	12.8(12.8)	7

[a] Estimation of second derivative through scale equal to a.

Table 7 contains the simulations of Table 5 but constrains the first two coefficients (c_0, c_1) to zero. The self-minimization still shows an excellent performance in reducing maximum errors in the whole domain of interest even in the presence of noise and forcing known boundary conditions. As in the case of Table 4, the computational effort is significantly reduced; however, in this case the symmetry among respective left–right coefficients cannot be seen due to the presence of noise.

Tables 8–10 illustrate the potential of the self-minimization when the third mode of a completely free beam (FF) is taken into account. These tables, similarly arranged as the previous respective tables, show the capability of method 2 to significantly reduce error estimations in the presence or in the absence of noise. With respect to these latter mentioned performances, Table 11 is worth mentioning. Table 11 takes into account the cases of Table 10 but constrains the last two coefficients (c_2, c_3) to zero. These constraints are consistent with the boundary conditions of a completely free beam requiring two natural conditions (global moment (y'') and shear (y''') nil). Firstly, the last cases do not seem to be in line with an improved first approximation (Max Error $[\%] = 25.4(3.16), 25.6(2.24)$); rather, the minimization outwardly provides a deterioration of the first approximation. However, this is effectively outward with respect to the real performance of the method, because the minimization is based on D_3 through a scale $a = 50$. In such a circumstance, because one of the boundary conditions regards D_3 (global shear nil), the minimization algorithm tries to change value and first derivative at the ends and introduces extremely small steps at the junctions which are mitigated by the large scale used ($a = 50$ means a wavelet having the extension of the domain of interest); these small steps are, however, raised by the inferior scale $a_2 = 20$ through Eq. (1). This interpretation is corroborated by the remaining simulations showing an identical maximum error between first approximation and self-minimization. Due to

Table 10
Performance method 2 on FF-III beam; $o_l = o_r = 10$; bounded; minimization based on D_3

a, a_2	$p_l(n)$				$p_r(n)$				Max Error[a] [%]	CPU time [s]
	c_0	c_1	c_2	c_3	c_0	c_1	c_2	c_3		
$S/N = 40$ dB										
20	1.0012	0.9996	1.5359	1.2972	0.9976	0.9538	2.0543	1.4140	32.7(17.45)	24
30	1.0020	1.0185	0.4153	0.7008	1.0002	0.9982	0.9431	0.7172	15.01(18.38)	28
50	1.0017	1.0139	0.6019	0.7655	1.0047	1.0395	0.3481	0.4963	12.57(21.03)	31
50, 20	=	=	=	=	=	=	=	=	5.30(17.45)	32
$S/N = 60$ dB										
20	1.0007	1.0064	0.7903	0.9449	1.0003	1.0020	0.9960	0.9928	6.93(7.139)	25
30	1.0003	1.0021	1.0231	1.0411	1.0002	1.0003	1.0654	1.0172	7.41(7.40)	19
50	1.0017	1.0102	0.8257	1.0110	1.0016	1.0104	0.7928	0.9522	12.76(12.76)	20
50, 20	=	=	=	=	=	=	=	=	5.33(7.14)	20

[a] Estimation of second derivative.

Table 11
Performance method 2 on FF-III beam; $o_l = o_r = 10$; bounded with $c_2 = c_3 = 0$; minimization based on D_3

a, a_2	$p_l(n)$				$p_r(n)$				Max Error[a] [%]	CPU time [s]
	c_0	c_1	c_2	c_3	c_0	c_1	c_2	c_3		
$S/N = 40$ dB										
20	0.9970	1.0071	0.00	0.00	1.0014	1.0288	0.00	0.00	3.16(3.16)	10
30	0.9807	0.9781	0.00	0.00	0.9858	1.0067	0.00	0.00	4.96(4.96)	9
50	0.8868	0.8737	0.00	0.00	0.8893	0.8993	0.00	0.00	12.6(12.6)	7
50, 20	=	=	=	=	=	=	=	=	25.4(3.16)	7
$S/N = 60$ dB										
20	0.9966	1.0014	0.00	0.00	0.9970	1.0035	0.00	0.00	2.24(2.24)	7
30	0.9814	0.9759	0.00	0.00	0.9819	0.9786	0.00	0.00	4.97(4.97)	8
50	0.8869	0.8724	0.00	0.00	0.8872	0.8749	0.00	0.00	12.8(12.8)	8
50, 20	=	=	=	=	=	=	=	=	25.6(2.24)	8

[a] Estimation of second derivative.

Table 12
Performance method 2 on CC,FF,SS-III beam; $o_l = o_r = 10$; a=50; $a_2 = 20$; bounded with $c_j = 0$; minimization based on D_4

BC	S/N	$p_l(n)$					$p_r(n)$					Max Error[a] [%]	CPU time [s]
		c_0	c_1	c_2	c_3	c_4	c_0	c_1	c_2	c_3	c_4		
CC	Noisy free	0.00	0.00	0.9486	0.8473	0.2954	0.00	0.00	0.9486	0.8473	0.2954	2.60(7.03)	21
$c_0 = c_1 = 0$	60 dB	0.00	0.00	0.9507	0.8548	0.3046	0.00	0.00	0.9578	0.8680	0.3144	2.58(6.80)	21
	40 dB	0.00	0.00	0.9704	0.9276	0.4165	0.00	0.00	1.0503	1.1151	0.7652	3.20(5.0)	23
FF	Noisy free	0.9847	0.9888	0.00	0.00	−2.0914	0.9847	0.9886	0.00	0.00	−2.0943	2.31(2.31)	16
$c_2 = c_3 = 0$	60 dB	0.9846	0.9888	0.00	0.00	−1.7776	0.9850	0.9917	0.00	0.00	−1.4725	2.24(2.24)	22
	40 dB	0.9841	0.9903	0.00	0.00	−0.7533	0.9879	1.0201	0.00	0.00	−0.4035	3.16(4.35)	20
SS	Noisy free	0.00	1.0082	0.00	0.9781	1.0491	0.00	1.0082	0.00	0.9781	1.0490	1.75(1.80)	14
$c_0 = c_2 = 0$	60 dB	0.00	1.0083	0.00	0.9593	0.9310	0.00	1.0118	0.00	0.9213	0.8083	1.83(2.60)	16
	40 dB	0.00	1.0086	0.00	0.8164	0.4562	0.00	1.0449	0.00	0.6045	0.2601	2.81(9.79)	19

[a] Estimation of second derivative.

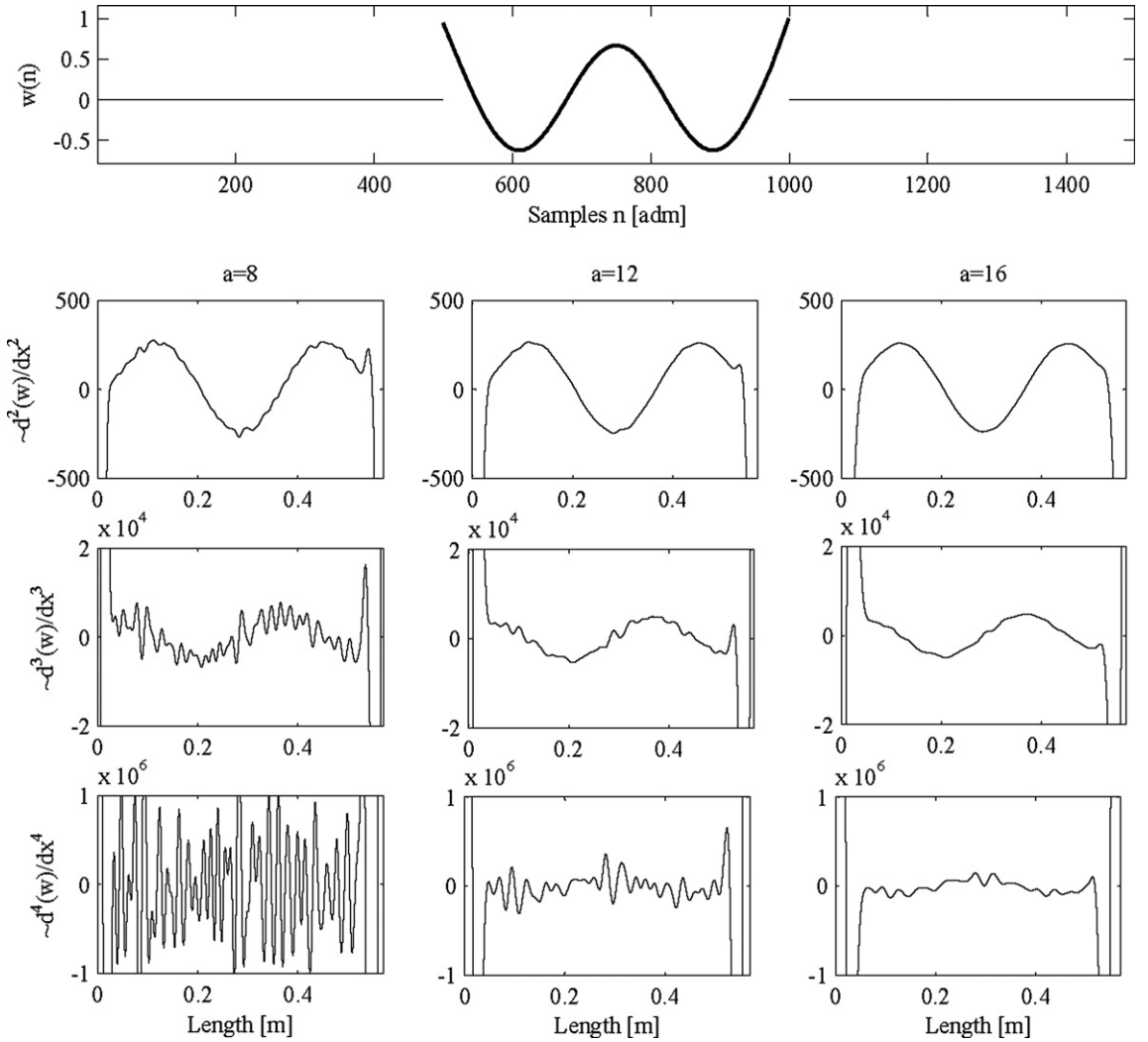

Fig. 13. Damage hidden by border distortion phenomenon; $L_c = 0.95 \cdot L$, $S/N = 53.98$ dB; third mode shape of a FF beam; extension by zero padding.

the peculiarity shown by this latter case, Table 12 is finally provided. Table 12 takes into account three classical boundary conditions when the minimization is carried out through D_4 and corrective coefficients are nullified depending on the respective adopted boundary conditions. Table 12 clearly shows stability with respect to any classical boundary condition and different levels of noise. The self-minimization provides an inferior or equal maximum percentage error compared to the first approximation; as far as the computational effort is concerned it is on average similar among the cases. It should be noticed that in the case of Table 12 the minimization is carried out on D_4, which, is an order of differentiation higher than anyone involved at the ends of the classical boundary conditions taken into account (CC, FF, SS).

5. Damaged beams, isomorphism and self-minimization on experimental and numerical tests

In this section, a number of simulations, showing the performance of both isomorphism and the self-minimization methods, aimed at reducing the border distortion phenomenon in damaged beams, are shown.

A first simulation is based on the code introduced in Gentile and Messina (2002); namely, damage is introduced close to the right end of a completely free beam ($L_c = 0.95 \cdot L$) and the third mode shape, corrupted by noise ($S/N = 53.98$ dB), is taken into account. Such a mode shape is shown with a bold line in the graph placed

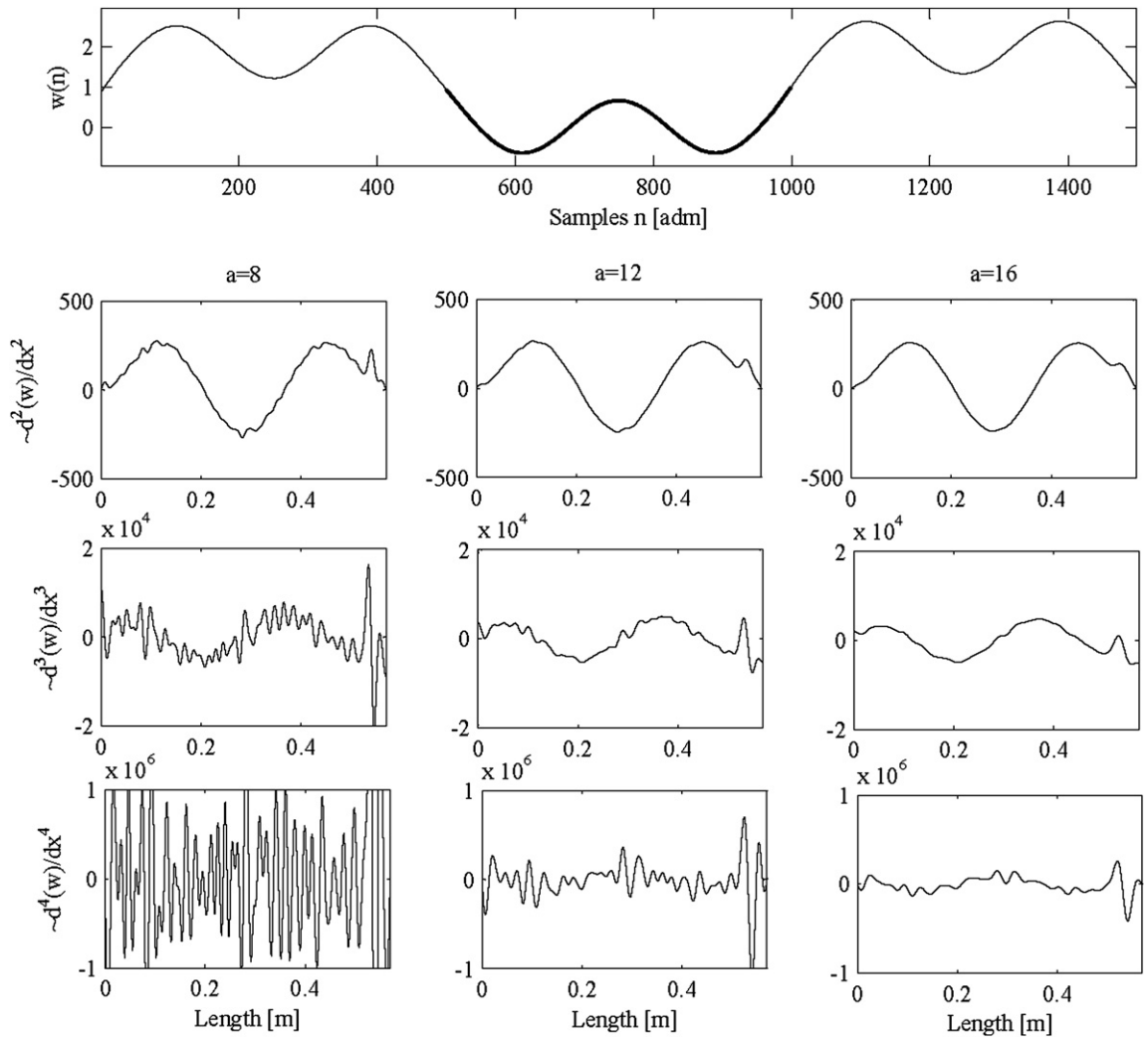

Fig. 14. Damage revealed by using isomorphism (*Rotation–Rotation*) (Ref. Fig. 13).

at the top of Fig. 13. This mode shape is extended by zero padding, which, for the application of (1) is equivalent to having no extension. The remaining nine graphs placed in Fig. 13 illustrate the influence of the scale on the second, third and fourth derivative obtained through convolution (1). These nine graphs also show a certain difficulty in identifying damage placed at $0.95 \cdot L$. In particular, when scale $a = 8$ is used a certain peak seems to be indicative of damage; however, it should be recognised that the corresponding peaks are confused by the rises of the $CWT_{2,3,4}$ at the ends. The peaks even disappear with higher scales ($a = 12$, 16) when trials aimed at reducing the noise are carried out.

Fig. 14 is arranged identically to Fig. 13, but now the extension is based on a rotation isomorphism at both ends. As is clear from Fig. 14 the damage condition is not hidden by any border distortion phenomenon. Indeed, the peak detecting the damaged condition is clearly detected at any level of scale. Similarly to Fig. 14, the graphs on the left of Fig. 15 show the second derivative estimated through the self-minimization method based on D_3 in comparison with the classical second derivative without any extension (these latter on

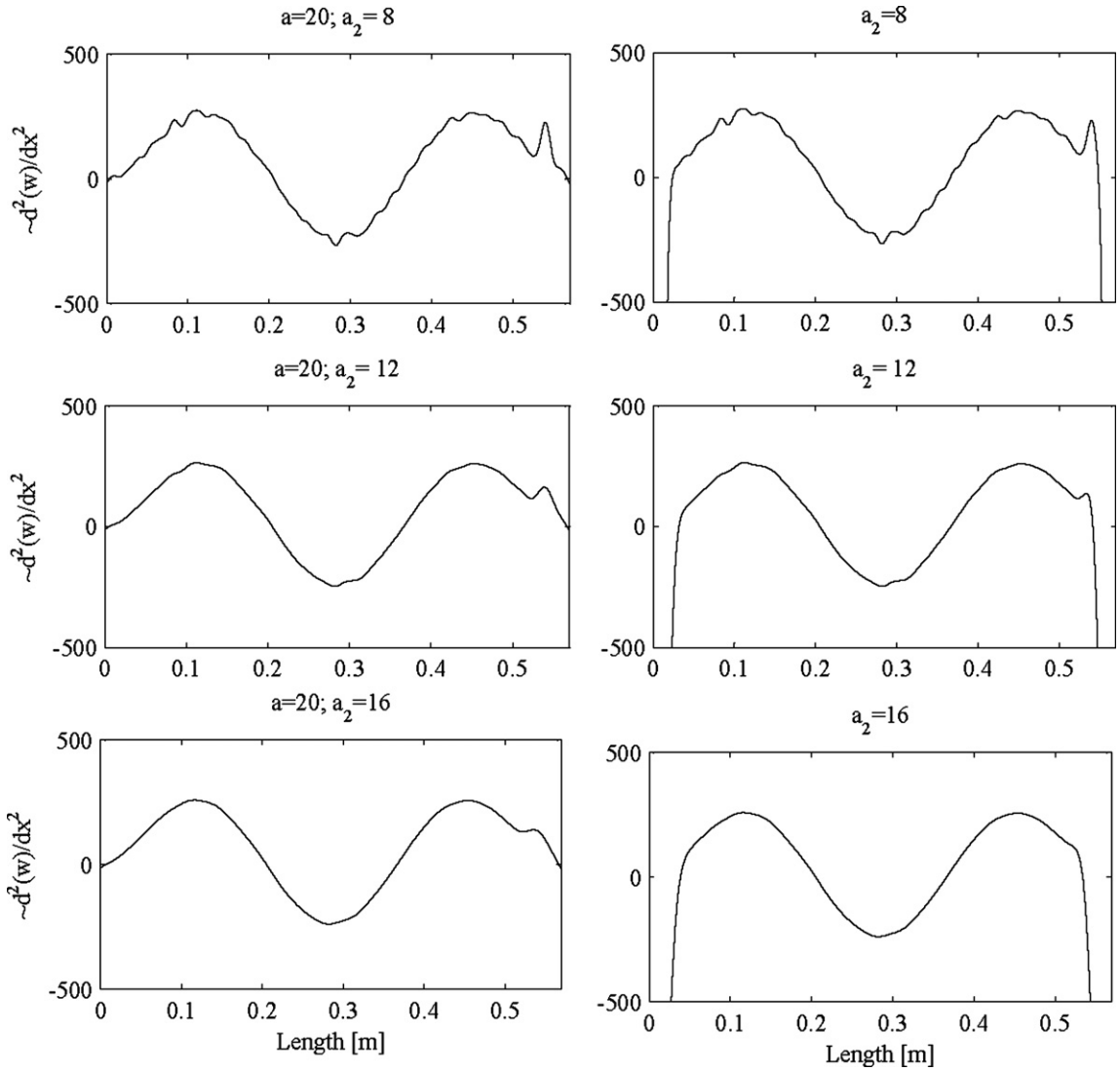

Fig. 15. Performance of self-minimization in the presence of boundary damage with $o_l = o_r = 10$; third mode shape of a FF beam (Ref. Fig. 13); bounded; minimization based on D_3.

the right of Fig. 15); clearly the self-minimization method preserves the damage state at any level of scale similarly to that of the rotation isomorphism.

Fig. 16 takes into account an experimental case described in Trentadue et al. (2007) and specifically the case depicted in Figs. 10 and 11 within the same reference. Firstly, it should be noticed that Fig. 16 does not show any false damaged condition as was established by an outlier contained in the original figures (Trentadue et al., 2007). This was possible by adopting the suggestions illustrated by Messina and Albanese (2008) in order to extract slightly improved dynamical shapes. Apart from this latter slight improvement it should be recognised as in Fig. 16, that the isomorphism eliminates an uncontrolled rise at the ends (right end, Figs. 10 and 11 in Trentadue et al. (2007)) and a false damaged condition (left-end, Figs. 10 and 11 in Trentadue et al. (2007)); moreover, the damage closer to the left-end ($n_c = 57$; Figs. 10 and 11 in Trentadue et al. (2007)) is more clearly detected as a real damaged condition through the second derivative rather than as a border distortion phenomenon. Before closing the discussion concerning Fig. 16, it should be noticed that a *Rotation* isomorphism was adopted at both the ends whilst, as discussed in Section 3.1, a *Turnover* transformation was judged to be more accurate for a clamped end. In truth, a turnover was tried but the rotation was able to pro-

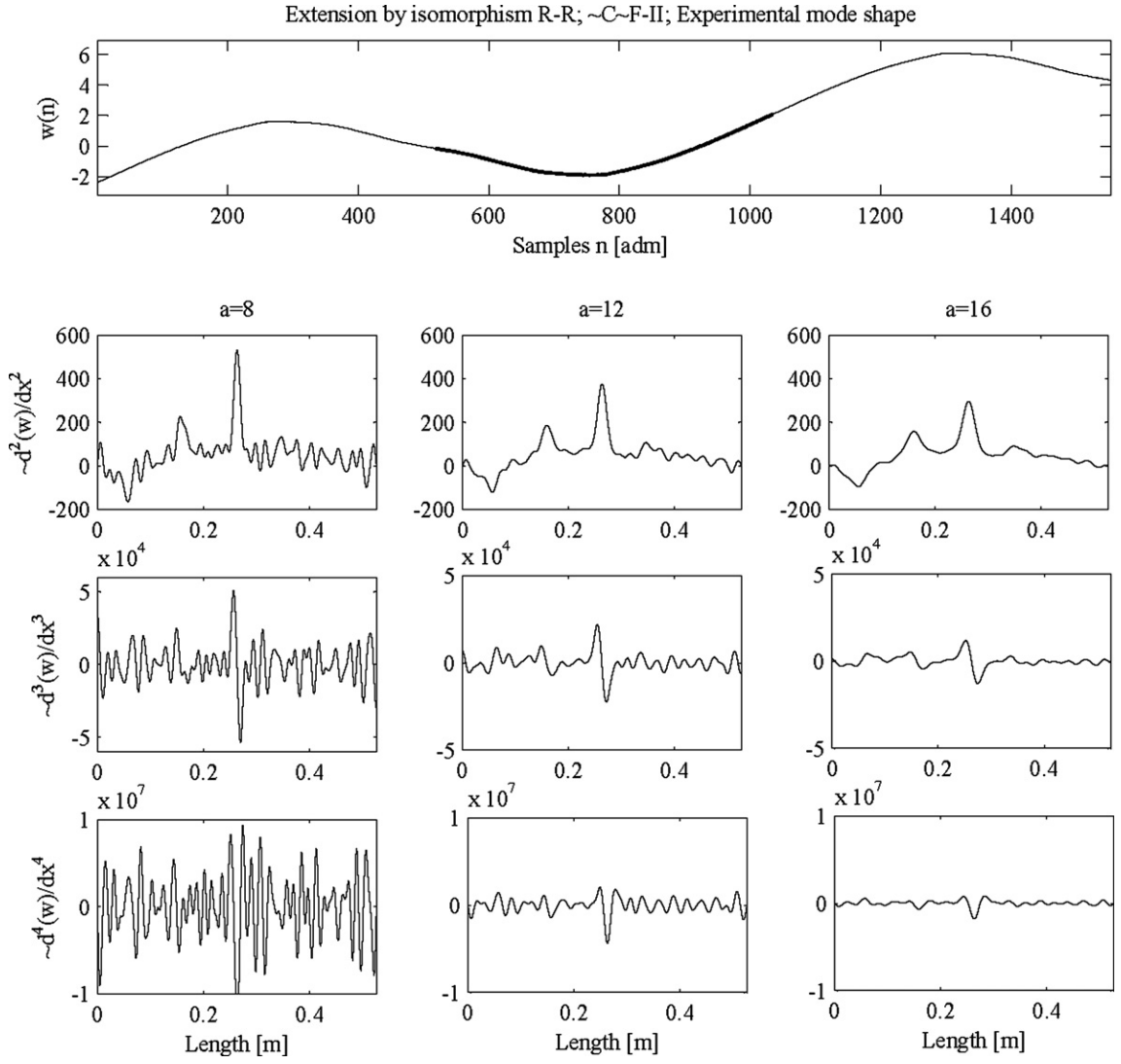

Fig. 16. CWT of an experimental dynamical shape (Figs. 10 and 11, Trentadue et al. (2007)) through convolution and R–R isomorphism.

vide a better result. This is not an unexpected behaviour because we are faced with an uncertain boundary condition; indeed, as is accurately explained in Trentadue et al. (2007), practical reasons did not allow the extension of the measurements up to the clamped or quasi-clamped end, and therefore, the measured ends results an uncertain boundary condition. In order to challenge the previously mentioned experimental case, the self-minimization method should not show difficulty to well perform a reduction of the border distortion phenomenon. In this respect, Fig. 17 should be taken into account. The minimization process (12) and (13) is in this case based on D_4 and the convolution (1) is carried out by adopting increasing scales from $a_{2,3} = 8$ up to 16 with step 4. Fig. 17 clearly shows for both second and third derivative the absence of any false damage indication and border distortion phenomenon within the whole domain of interest.

In order to complete the comparison between isomorphism and self-minimization, Fig. 18 is finally provided to compare with Fig. 14. The minimization process (12) and (13) regarding Fig. 18 is based on D_4 and the convolution (1) is carried out by adopting increasing scales from $a_{2,3} = 8$ up to 16 with step 4.

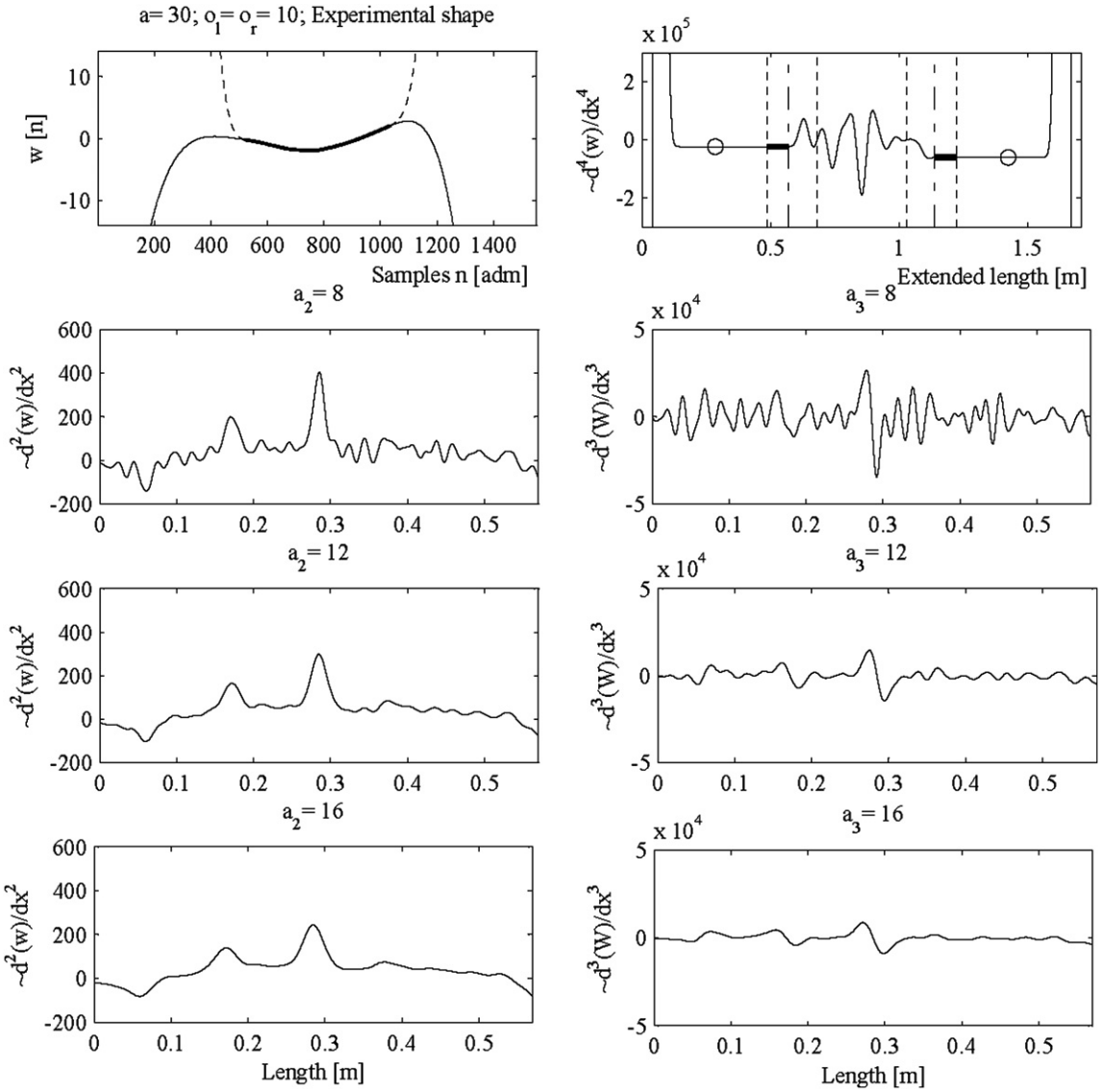

Fig. 17. Performance of self-minimization with $o_l = o_r = 10$; experimental dynamical shape (Figs. 10 and 11, Trentadue et al. (2007)); bounded; minimization based on D_4.

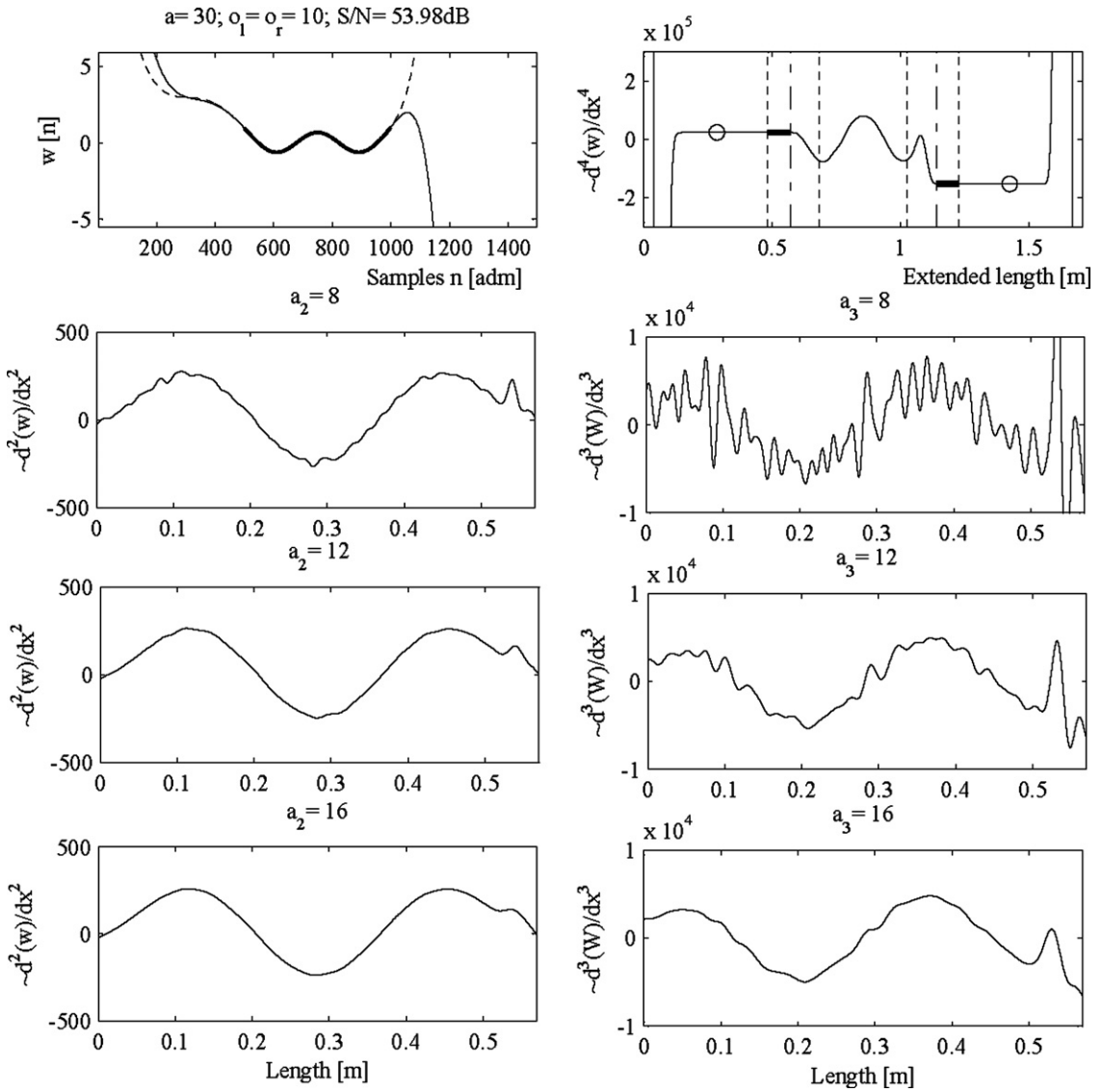

Fig. 18. Performance of self-minimization in the presence of boundary damage with $o_l = o_r = 10$; third mode shape of a FF beam (Ref. Fig. 13); bounded; minimization based on D_4.

Fig. 18 still clearly shows for both second and third derivative the absence of any false damage indication and a strong reduction in the border distortion phenomenon within the whole domain of interest which allows the detection of a damaged condition at $0.95 \cdot L$.

6. Conclusions

In this work, two different methods aimed at challenging the known phenomenon of border distortion concerning the use of wavelets, when these latter are used in the guise of continuous wavelet transforms (cwt) for identifying damage on transversally vibrating structural components (e.g., beams, plates and shells), have been introduced. Both the methods have been theoretically discussed and their performances have been accurately tested against several numerical and experimental tests in the presence or absence of noise. All the simulations have shown the robustness of both methods.

The first method (based on isomorphism) should always be preferred to the second one (method 2 or self-minimization) due to its straightforward application and extreme robustness against any level of noise; the method is also characterized by a negligible computational effort. Moreover, the great advantage of method 1 which is aimed at avoiding any extrapolating techniques should not be neglected. A table suggesting the use of method 1, in relation to specific classical-beam boundary conditions, has also been provided.

The second method can decisively assist in all cases where uncertain boundary conditions and poor results are obtained by the above mentioned *Rotation* and *Turnover* transformations. In particular, the presence of uncertain boundary conditions or more complicated structural components (as plates an shells) can occur in practice; in this respect the classical geometrical and/or natural boundary conditions (C, F, S) adopted in the relevant sections of this manuscript should be able to guide the choice of the analyst between methods 1 and 2.

The robustness of method 2 against noise (even with $S/N = 40$ dB) and different geometric cases and several boundary conditions has also been tested. Method 2 offers different chances to the analyst: the minimization can be carried out on high differentiation orders in order to ensure continuity at lower differential orders and, therefore, reductions in the border distortion and false damage detections can be expected; different use of scales is also possible in the sense that large scales can smooth the differentiations and ensure a stronger reduction in the border distortion but clearer details can be recovered by convolving the extended signal with lower scales. All these performances can be carried out regardless of the particular boundary conditions involved. However, the computational effort accompanying this method cannot be neglected. Indeed, on average all the simulations involved a computational effort of few 10ths of a second per beam.

In spite of the fact that the negative influence of the phenomenon regarding the border distortion has been recognized in the past, it has never received appropriate specific attention; in this respect this is the first work dealing with the phenomenon which introduces two methods showing interesting performances and covering the majority of real cases occurring in practice.

References

Dimarogonas, A.D., 1996. Vibration of cracked structures: a state of the art review. Engineering Fracture Mechanics 55, 831–857.

Di Sante, R., Messina, A., Cavaccini, G., Pianese, V., 2008. Structural damage detection in composite aeronautical components through methods based on digital filtering and wavelet transforms. In: Seventh European Conference on structural Dynamics (EURODYN 2008), Southampton (UK).

Doebling, S.W., Farrar, C.R., Prime, M.B., 1998. A summary review of vibration-based damage identification methods. The Shock and Vibration Digest 30, 91–105.

Gill, P.E., Murray, W., Wright, M.H., 1995. Practical Optimization. Academic Press, New York.

Gentile, A., Messina, A., 2002. Detection of cracks by only measured mode shapes in damaged conditions. In: Proceedings of the third Interference Conference in Identification in Engineering Systems (UK) Swansea (UK), pp. 208–220, ISBN: 0860761754.

Gentile, A., Messina, A., 2003. On the continuous wavelet transforms applied to discrete vibrational data for detecting open cracks in damaged beams. International Journal of Solids and Structures 40, 295–315.

Han, J.-G., Ren, W-X., Sun, Z.-S., 2005. Wavelet packet based damage identification of beam structures. International Journal of Solid and Structures 42, 6610–6627.

Hong, J.C., Kim, Y.Y., Lee, H.C., Lee, Y.W., 2002. Damage detection using the Lipschitz exponent estimated by the wavelet transform: applications to vibration modes of a beam. International Journal of Solids and Structures 39, 1803–1816.

Kim, H., Melhem, H., 2004. Damage detection of structures by wavelet analysis. Engineering Structures 26, 347–362.

Lee, T.C.M., Oh, H.-S., 2004. Automatic polynomial wavelet regression. Statistics and Computing 14, 337–341.

Loutridis, S., Douka, E., Trochidis, A., 2004. Crack identification in double-cracked beams using wavelet analysis. Journal of Sound and Vibration 277, 1025–1039.

Mallat, S., 2001. A Wavelet Tour of Signal Processing. Academic Press, New York.

Messina, A., 2004. Detecting damage in beams through digital differentiator filters and continuous wavelet transforms. Journal of Sound and Vibration 272, 385–412.

Messina, A., Albanese, A., 2008. A consistent estimator of dynamic shapes at high signal/noise ratio within the area of damage detection. In: Seventh European Conference on structural Dynamics (EURODYN 2008), Southampton, UK.

Misiti, M., Misiti, Y., Oppenheim, G., Poggi, J., Rel.2006b, Ver. 3.1. Wavelet toolbox for use with MATLAB, Natick, MA, USA.

Oh, H.-S., Lee, T.C.M., 2005. Hybrid local polynomial wavelet shrinkage: wavelet regression with automatic boundary adjustment. Computational Statistics & Data Analysis 48, 809–819.

Oh, H.-S., Naveau, P., Lee, G., 2001. Polynomial boundary treatment for wavelet regression. Biometrika 88, 291–298.

Pandey, A.K., Biswas, M., Samman, M.M., 1991. Damage detection from changes in curvature mode shapes. Journal of Sound and Vibration 145, 321–332.

Ratcliffe, C.P., 1997. Damage detection using a modified Laplacian operator on mode shape data. Journal of Sound and Vibration 204, 505–517.

Ratcliffe, C.P., Bagaria, W.J., 1998. Vibration technique dor locating delamination in a composite beam. AIAA Journal 36, 1074–1077.

Reese, R.T., Kawahara, W.A., 1993. Handbook on Structural Testing. SEM, The Fairmont Press, Inc. 700 Indian Trail, Liburn, GA 30247.

Rucka, M., Wilde, K., 2006a. Application of continuous wavelet transform in vibration based damage detection method for beams and plates. Journal of Sound and Vibration 297, 536–550.

Rucka, M., Wilde, K., 2006b. Crack identification using wavelets on experimental static deflection profiles. Engineering Structures 28, 279–288.

Salawu, O.S., 1997. Detection of structural damage through changes in frequency: a review. Engineering Structures 19, 718–723.

Staszewski, W.J., Boller, C., Tomlinson, G.R., 2004. Health Monitoring of Aerospace Structures. John Wiley & Sins, Ltd..

Strang, G., Nguyen, T., 1996. Wavelets and Filter Banks. Wellesley-Cambridge Press.

The MathWorks, Rel.2006b, Ver.3.1. Optimization toolbox for use with MATLAB, Natick, MA, USA.

Trentadue, B., Messina, A., Giannoccaro, N.I., 2007. Detecting damage through the processing of dynamic shapes measured by a PSD-triangular laser sensor. International Journal of Solids and Structures 44, 5554–5575.

Wang, Q., Deng, X., 1999. Damage detection with spatial wavelets. International Journal of Solids and Structures 36, 3443–3468.

Yoon, M.K., Heider, D., Gillespie Jr., J.W., Ratcliffe, C.P., Crane, R.M., 2005. Local damage detection using the two-dimensional gapped smoothing method. Journal of Sound and Vibration 279, 119–139.

Yuen, M.M.F., 1985. A numerical study of the eigenparameters of a damaged cantilever. Journal of Sound and Vibration 103, 301–310.